METEOROID IMPACT DETECTION FOR EXPLORATION OF ASTEROIDS (MIDEA)

NIAC Phase I Final Report

Grant number 80NSSC18K0873

Nicolas Lee and Sigrid Close (PI)

Stanford University

2019 March 25

Abstract

Asteroids contain a wealth of resources including water and precious metals that can be extracted. These resources could be applied to in-space manufacture of products that depend less on material launched from Earth's surface. The Meteoroid Impact Detection for Exploration of Asteroids (MIDEA) concept addresses the challenge of characterizing an asteroid surface using a small satellite with a constellation of free-flying plasma sensors to assess the asteroid's viability for in situ resource utilization (ISRU). The plasma sensors detect ions ejected from the surface of an asteroid by meteoroid impacts, enabling the surface composition to be inferred.

The objective of this NIAC Phase I study was to demonstrate feasibility of the MIDEA architecture in the context of proximity operations around an asteroid target and to develop the design of an orbital geometry and attitude control strategy for the ultralight plasma sensors. This was undertaken through a simulation framework to identify and characterize a favorable orbit for the MIDEA sensor constellation, and developing a sensor geometry that is consistent with maintaining the pointing requirements necessary to operate with sufficient power generation.

Our study showed that a polar orbit aligned along the asteroid terminator provided sufficient stability for the sensors in the low gravitational environment under the influence of substantial solar radiation pressure. Reflector vanes using controlled reflectivity devices implemented with liquid crystal technology are capable of maintaining the sensor attitude so that it consistently points its solar panels in the sun direction and the sensor electrode at the asteroid surface. Finally, the reduction in meteoroid impact detection due to visibility constraints from the proposed orbit does not substantially extend the expected mission duration.

These results indicate that the MIDEA concept can be achievable using a 10–20 kg spacecraft, which would be able to characterize the surface composition of an asteroid within 30–50 days of proximity operations. This architecture, implemented in parallel to multiple asteroid targets, would enable widespread exploration of near-Earth asteroids at low cost.

Table of contents

List of figures

1   Introduction

The *Meteoroid Impact Detection for Exploration of Asteroids* (MIDEA) architecture leverages the natural space environment in order to provide a continuous source of meteoroid impacts, resulting in erosion of the material on the asteroid surface [*Lee and Close*, 2017]. These impacts produce a plasma that expands outward into space and provide information on the composition of the asteroid surface. The goal of MIDEA is to enable low-cost exploration of small (100−1000 m) near-Earth asteroids (NEA) using a parent spacecraft in the 10−50 kg range, carrying a constellation of free-flying ultralight plasma sensors to study the transient plasma environment in the asteroid's vicinity. In the context of a reference mission to a near-Earth asteroid (NEA), we focus on the design of the lightweight spacecraft configuration required to achieve sufficient performance in power generation and attitude control. In particular, we focus on a mission to 2008 EV5, a 450 m C-type (carbonaceous) asteroid, which was the reference target for the Asteroid Redirect Mission [*Mazanek et al.*, 2014].

1.1   Overview of the MIDEA architecture

The MIDEA concept proposes to launch a batch of small spacecraft (such as a 6U or 12U CubeSat with an external orbit insertion motor) and send them individually to a set of asteroid targets, where each deploys a constellation of ultralight plasma sensors. These free-flying plasma sensors detect the expanding ions produced by a meteoroid impact on the surface of an asteroid. Because of the transient nature of impact plasmas, conventional plasma instruments are insufficient to determine the ion composition. However, the MIDEA concept extends the principle of time-of-flight mass spectroscopy by measuring the time of flight of ions over the 100–300 m distance from the asteroid surface to the orbiting sensors. Using this technique, the mass of the ions can be inferred, and they can be traced back to the point of impact to construct a composition map of the asteroid surface. The parent spacecraft tracks the location of the deployed sensors and the impact plasma detection events, constructing a map of the composition of the asteroid surface.
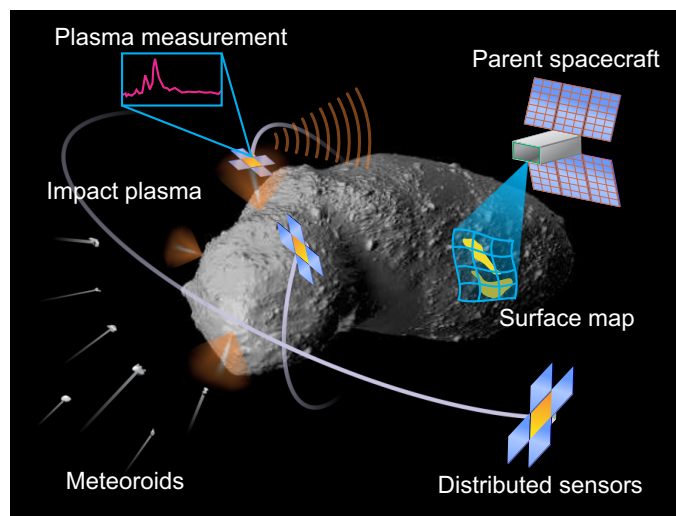
Figure 1: Overview of the MIDEA system concept.

The plasma sensors are each free-flying, and therefore require independent spacecraft systems such as power, communications, and attitude control. Recent developments in chipsats have resulted in spacecraft bus designs, including command and data handling, electrical power system, photovoltaic cells, and communications, that are approximately 5 g in mass [*Manchester et al.*, 2013]. Attitude control of these lightweight spacecraft can be achieved through controlled reflectivity using thin-film liquid crystal devices (LCDs) [*Saiki et al.*, 2012], and passively through design of the spacecraft geometry [*Atchison and Peck*, 2010]. Each sensor will deploy to an area of at least 50 cm^2 to produce on the order of 1–5 W. The deployable panels could be similar in design to the ultralight membrane concentrators envisioned for space solar power satellites, which are 10×10 cm with a prototype mass of 1.5 g [*Arya et al.*, 2016].

The plasma sensor itself is an electrostatic probe, consisting of a metallic collector plate on which the incoming ions deposit a current, and a transimpedance amplifier of sufficient gain to convert the current into a voltage signal [*Goel et al.*, 2015]. The expected current pulse deposited by the ions from a nanogram impact is on the order of picoamperes to nanoamperes at a distance of 100 m. To determine ion mass, the time of flight from the point of impact to the sensor location must be established. This can be accomplished through optical detection of the impact flash on the asteroid surface or through multiple detections of the ion plume using different sensors. Based on estimates of the expansion speed, millisecond-level timing is required to provide sufficient mass resolution for determining ion composition. Upon detection of a plasma pulse, the sensor would compute the times and amplitudes of signal peaks and report these to the parent spacecraft.

The parent spacecraft is responsible for orbit insertion at the asteroid, deploying the sensors into their orbits, and synthesizing the impact detections into a coherent data package for transmission to Earth. The required bandwidth is not large, and could be transmitted through a planar reflectarray antenna derived from the ISARA or MarCO designs [*Hodges et al.*, 2015]. A minimal design could be as small as a 6U CubeSat, with 1U each allocated to power, propulsion, data handling, attitude control, communications, and sensors, with an external motor for insertion. Propulsion systems for CubeSats and other nanosatellites do not have much flight heritage to date, but numerous competing technologies are in development that could achieve this delta V, including hybrid rockets [*Jens et al.*, 2014; *McKnight et al.*, 2014; *Jansen et al.*, 2012], electrospray ion thrusters [*Martel et al.*, 2012], and RF ion thrusters [*Kolosa et al.*, 2014; *Sheehan et al.*, 2014]. After deploying the plasma sensors into their designated orbits, the nominal position of the parent spacecraft is to hover over the sunlit portion of the asteroid, and requires a constant thrust to offset the gravitational pull. Assuming a 200 m asteroid with a density of 2000 kg m^{-3}, a 20 kg spacecraft at 200 m altitude would require 0.28 mN of thrust. This could be achieved using a 2 kV electrospray thruster, providing 5000 s specific impulse and a fuel consumption of 0.01 mg s^{-1} or 26 grams per month [*Velasquez-Garcia et al.*, 2006].

1.2   Summary of NIAC Phase I results

This NIAC Phase I study built upon prior work designing the plasma sensor for the MIDEA concept through a NASA Early Stage Innovations (ESI) grant. Key results from the ESI work include characterization of plasma plume geometry (Sections 4.1.1 and 4.1.2) and impact rates (Section 4.2.2), as well as a preliminary design of the ultralight plasma sensor. The NIAC study identified propulsion requirements for rendezvous with asteroid 2008 EV5 and analyzed the orbital dynamics, sensor geometry, and attitude control requirements needed to achieve the MIDEA mission objectives.

The key findings from this NIAC study include the following:

- A 2024–2026 mission to 2008 EV5 can be accomplished with post-insertion delta V of 0.45 km/s.
- The ultralight plasma sensors must be deployed into a polar terminator orbit to maintain stability over the duration of the mission.
- The design mass of the plasma sensors must be increased to 250 g for robustness against uncertainties in the total asteroid mass.
- Controlled reflectivity provides sufficient actuation authority to maintain attitude control of the plasma sensors.
- The total required mission duration is not substantially increased by consideration of orbital constraints.

1.3   Report outline

The remainder of this report is organized as follows. Section 2 provides background on the relevant topics related to asteroid classification and exploration, as well as a review of relevant prior NIAC studies. Section 3 discusses the study of MIDEA's orbital dynamics and sensor constellation placement. Section 4 reviews our prior work on hypervelocity plasma expansion and applies this analysis to asteroid 2008 EV5, including the modifications to the prediction of meteoroid impact rate that account for observability limitations due to orbital constraints. Section 5 summarizes the main findings and provides possible directions for future work.

2   Background

2.1   Asteroid and meteoroid classification

Asteroids are categorized by spectral type and partitioned into different families based on orbits. The spectral type of an asteroid is assigned based on Earth-based telescope observations. Several taxonomic systems are in use [*Chapman et al.*, 1975; *Zellner et al.*, 1985; *Bus and Binzel*, 2002], but most asteroids fall in broad categories for C (carbonaceous), S (stony), and X (other) asteroids. The spectral type corresponds to the surface composition of the asteroid and suggests the abundance of materials available for in situ resource utilization (ISRU).

Near-Earth asteroids (NEAs), with orbits close to or crossing 1 AU in radius, are of primary interest for ISRU because of the lower fuel requirements for rendezvous compared to asteroids further away. The number of NEAs greater than 100 m in size is estimated to be approximately 20,000, based on a synthetic population that corresponds to the detection rate of the NEOWISE mission [*Mainzer et al.*, 2011]. The main-belt asteroids orbiting between Mars and Jupiter are potential ISRU targets for the distant future, especially for applications where the resources do not need to be returned to Earth. The number of asteroids between 1 and 2 km in diameter is estimated to be over 900,000 [*Bottke et al.*, 2005] and follows a power law with a size index of -3.5 [*O'Brien and Greenberg*, 2005], indicating that there may be as many as ten million asteroids in the main belt in MIDEA's 100–300 m size range.

Asteroids are airless bodies and their surface conditions are strongly influenced by the space environment. The flow of the solar wind around asteroids can produce plasma wakes, while photoemission on sunlit surfaces liberates electrons. Particle-in-cell simulations have shown that NEAs can sustain an outward-pointing electric field of approximately 1 V/m on the sunlit faces [*Zimmerman et al.*, 2014], which would enhance the separation of an impact plasma and repel the positively charged ions from the asteroid surface.

Meteoroids are naturally occurring, solid objects moving in interplanetary space, ranging in size from 100 μm to 10 m [*Beech and Steel*, 1995]. Smaller particles, known as dust, are differentiated from meteoroids because of the different physics involved in their passage through the Earth's atmosphere. However, in this paper we will refer to all small, naturally occurring solid bodies as meteoroids, since there is no clear delineation between dust and meteoroids in terms of impact physics. The speed of interplanetary meteoroids is constrained by the heliocentric escape velocity, corresponding to approximately 42, 30, and 24 km/s at distances of 1, 2, and 3 AU from the sun, respectively.

2.2   Relevance to NASA, scientific community, and society

The principal impact of this concept is to enable low-cost exploration of asteroids using small satellites. While the primary objective of MIDEA is to support ISRU efforts, the concept will also yield peripheral data such as counts of meteoroid impacts, which could then be used to refine existing meteoroid population models. Current meteoroid models are poorly constrained beyond the orbit of Mars, due to scarcity of data [*National Research Council*, 2011a]. If this technology is used to survey asteroids in the main belt, it will offer a dramatic increase in the availability of meteoroid flux measurements in deep space. These measurements will be especially critical for mission assurance if a subsequent manned or high-cost ISRU mission is planned to arrive at the same asteroid.

Knowledge of the deep space meteoroid environment will not only benefit future mission safety, but has the potential to address several scientific questions. Infrared emission from dust sources is a known noise source for cosmological studies of the cosmic microwave background [*Schlegel et al.*, 1998; *Li and Draine*, 2001] and could be better characterized with measurements

of meteoroid flux. Identification of and discrimination between interstellar and interplanetary dust particles through estimation of impact velocity can provide insight into the composition of the interstellar medium [e.g., *Draine*, 2003].

The MIDEA architecture supports NASA's 2018 Strategic Plan Objectives 1.1, 3.1, and 4.3 by enabling exploration capabilities that will provide an improved understanding of asteroids while yielding data that will improve future mission safety. It is also well aligned with the following areas of NASA's 2015 Technology Roadmap:

- 7.1 In situ resource utilization - reconnaissance, prospecting, mapping;
- 7.5 Mission operations and safety - risk assessment tools; and
- 8.3 In situ instruments and sensors.

The benefits of the proposed work extend beyond NASA, in that the mission concept would enable commercial entities to pursue their own missions to explore asteroids for ISRU. Scientific interest in the exploration of small bodies is reflected in its relevance to five out of the ten priority questions identified in the planetary science decadal survey [*National Research Council*, 2011b]. Public interest in both asteroid exploration and commercial space are both intrinsically high, especially with the recent discovery of the interstellar object 'Oumuamua [*Meech et al.*, 2017]. Finally, the study of navigation strategies for ultralight spacecraft will be complementary to other long-term goals in space exploration, including the development of femtosatellites, which are much more dependent on orbital maneuvers using solar radiation pressure, and the implementation of solar sails and light sails for planetary and interstellar exploration [*Simmons and McInnes*, 1993].

2.3 Exploration missions to asteroids

Prior in situ exploration of asteroids and comets has primarily been conducted using single-spacecraft missions, occasionally carrying an impactor or lander that is deployed from the primary spacecraft. Most have carried some form of spectrographic instrumentation for studying the composition of the surface. Examples include Dawn, which visited Vesta in 2011–2012 and is currently orbiting Ceres [*Russell and Raymond*, 2011], and NEAR Shoemaker, which visited Eros in 2001 [*Santo et al.*, 1995].

The Dawn spacecraft carried a visible-to-near-IR camera, a visible-to-IR spectrometer, and a gamma ray and neutron detector, with masses of 5.5 kg, 20 kg, and 9.4 kg, respectively, and power consumptions rated at 17 W, 52 W, and 15 W [*Pieters et al.*, 2011; *Sierks et al.*, 2011; *De Sanctis et al.*, 2011; *Prettyman et al.*, 2011]. The NEAR spacecraft carried a multi-spectral imager, near-infrared imaging spectrograph, and x-ray/gamma-ray spectrograph, with masses and power consumptions of 7.8 kg, 13.9 W; 14.2 kg, 20.0 W; and 27.3 kg, 31.3 W, respectively [*Santo et al.*, 1995]. More recently, the OSIRIS-REx spacecraft includes three spectrometers for identifying mineral and organic composition of the surface of asteroid Bennu [*Beshore et al.*, 2015]. These include a visible and IR spectrometer, a thermal emission spectrometer, and an X-ray imaging spectrometer.

Spectrometers have also been used on Mars missions, including on the Mars Exploration Rovers and on Curiosity [*Squyres et al.*, 2006; *Gellert et al.*, 2015]. Curiosity's ChemCam instrument includes a laser-induced breakdown spectrometer, which can be used to target specific sample locations. This targeting ability would be beneficial compared to relying on meteoroid impacts for efficiently surveying an asteroid surface, but the power and optical aperture needed to focus such a laser might be infeasible.

Some of these instruments have miniaturized equivalents that are being developed for flight on CubeSats but spectrometers tend to be challenging to miniaturize compared to field and particle instruments [*Castillo-Rogez*, 2015]. Additionally, the processes governing spectroscopic measurements are limited by the optical resolution of the instrument, resulting in an averaged measurement at the spatial resolution on the asteroid surface, which is typically on the order of 1 m. In contrast, MIDEA's impact plasma measurement provides the ability to determine the surface composition at a micron scale, which would provide a better indication of the heterogeneity of the surface.

2.4   NIAC studies relevant to MIDEA

As a concept to enable broad exploration of NEAs, the MIDEA architecture stands to benefit from developments in small satellite technologies and deep space propulsion, and is complementary to related mission architectures focused on the exploration and exploitation of asteroids and the resources they contain. The NIAC program has yielded many such studies, some of which are discussed here in the context of their relationship to the MIDEA study.

In terms of small satellite technologies that would increase the capabilities of MIDEA directly, the components and systems analyzed in the Branecraft concept [*Janson*, 2017] and techniques proposed for 2D planetary surface landers [*Hemmati et al.*, 2014] are applicable to the design and manufacture of MIDEA's ultralight plasma sensors, and the development of a system for plasmonic force propulsion [*Rovey et al.*, 2014] could enhance the maneuverability of the mothership and correspondingly the precision of MIDEA's sensor deployment. The Comet hitchhiker concept [*Ono et al.*, 2015] could be harnessed to provide sufficient delta V for a single MIDEA launch to reach multiple asteroid targets without increasing the propulsive needs of a secondary boost stage.

The MIDEA architecture need not be a stand-alone mission, and could be flown as one payload with other systems providing complementary science measurements such as those returned by neutron activated analysis from a CubeSat lander [*Wang et al.*, 2015], seismic exploration [*Plescia*, 2016], quantum inertial gravimetry [*Streetman et al.*, 2015], muography using galactic cosmic ray showers [*Prettyman et al.*, 2014], or swarm flyby gravimetry [*Atchison et al.*, 2015; 2017]. In particular, the use of gravimetry based on the trajectory of the mothership or an initially deployed plasma sensor could inform the deployment strategy of the susbsequent sensors in the constellation to maximize orbital stability. Follow-on missions to targets identified by MIDEA as attractive for resource utilization could include the WRANGLER architecture to capture and de-spin an asteroid

[*Hoyt et al.*, 2015] or a robotic asteroid prospector [*Cohen et al.*, 2013], potentially leading to the in-space manufacture of propellants from asteroids [*Lewis*, 2016] or extraction of water for human consumption or radiation shielding [*Sercel*, 2016].

This family of NIAC studies provides a comprehensive effort toward enabling widespread asteroid exploration and resource utilization with many complementary technologies that can be concurrently developed.

3   Dynamics of the sensor spacecraft

The primary goal of this NIAC study was to understand the orbital dynamics associated with the MIDEA architecture and the implications of these constraints on the overall mission. In this section, we address the heliocentric cruise phase of the mission in Section 3.1, orbits of the plasma sensor spacecraft around the asteroid in Section 3.2, and sensor attitude control in Section 3.3.

3.1   Asteroid rendezvous trajectories

Asteroid 2008 EV5, a 450 m C-type (carbonaceous) asteroid that was one of the reference targets for the Asteroid Redirect Mission [*Mazanek et al.*, 2014], was selected for this study as an asteroid candidate with a benign (roughly spherical) geometry and suitable size range for the MIDEA concept. The NASA Ames Trajectory Browser (available at trajbrowser.arc.nasa.gov) was used to enumerate rendezvous trajectories that could be used to estimate propulsive requirements for Earth escape and heliocentric orbit insertion, as well as for asteroid capture. Figure 2 summarizes the rendezvous trajectory parameters from which an optimal candidate solution was selected. The selected trajectory, with an Earth departure on 2024 Dec 20 and arrival on 2026 Aug 04, had the lowest post-insertion delta V of 0.450 km/s required at asteroid rendezvous, and a total delta V of 4.04 km/s including Earth escape. This asteroid rendezvous delta V is achievable using a hybrid propulsion system currently under development that would provide up to 0.8 km/s delta V within a 12U CubeSat envelope [*Jens et al.*, 2018].
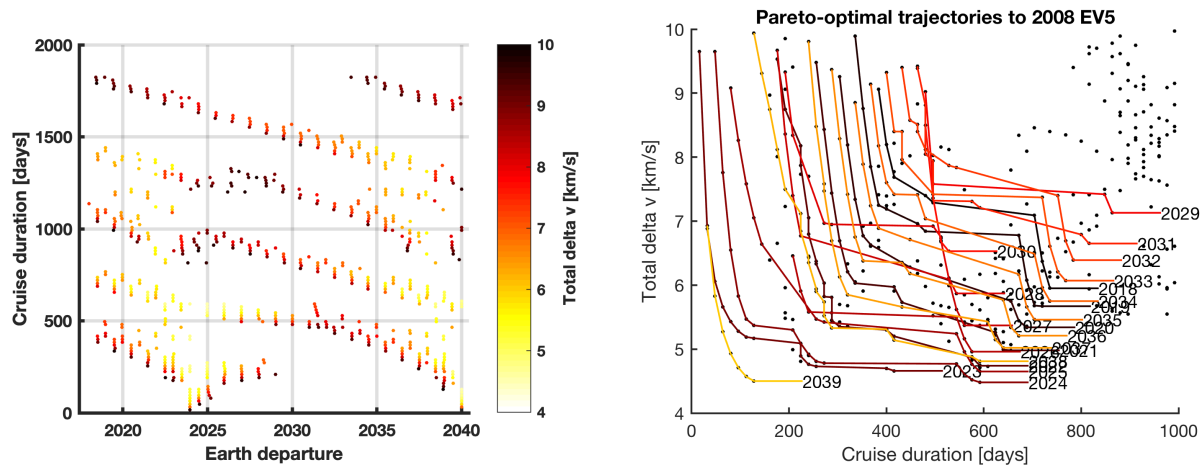
Figure 2: Propulsion requirements for rendezvous with 2008 EV5. Total delta V and cruise duration as a function of Earth departure date (left) and annual pareto-optimal trajectories with respect to total delta V and cruise duration (right).

3.2   Orbits around small bodies

In assessing the feasibility of the proposed MIDEA mission to 2008 EV5, proximity operations around the asteroid were the major challenge addressed during the Phase I study. In particular, our goal was to identify orbits that did not require constant thrust, to minimize the control effort required of the plasma sensor spacecraft. Because of the substantial solar radiation pressure perturbation compared to the asteroidal gravitational acceleration, the family of sun-synchronous polar orbits identified by *Scheeres* [1999] and *Morrow et al.* [2001] was analyzed in a numerical simulation using MIDEA-relevant spacecraft parameters.

Figure 3 illustrates the nominal 400 m polar orbit under consideration, viewed from an inertial frame and a rotating sun-synchronous frame. In the sun-synchronous rotating frame, the orbit exhibits some variation but maintains its approximate alignment with the asteroid terminator (the boundary between the sunlit and dark sides of the asteroid) with limited deviation in the radial and out-of-plane directions.
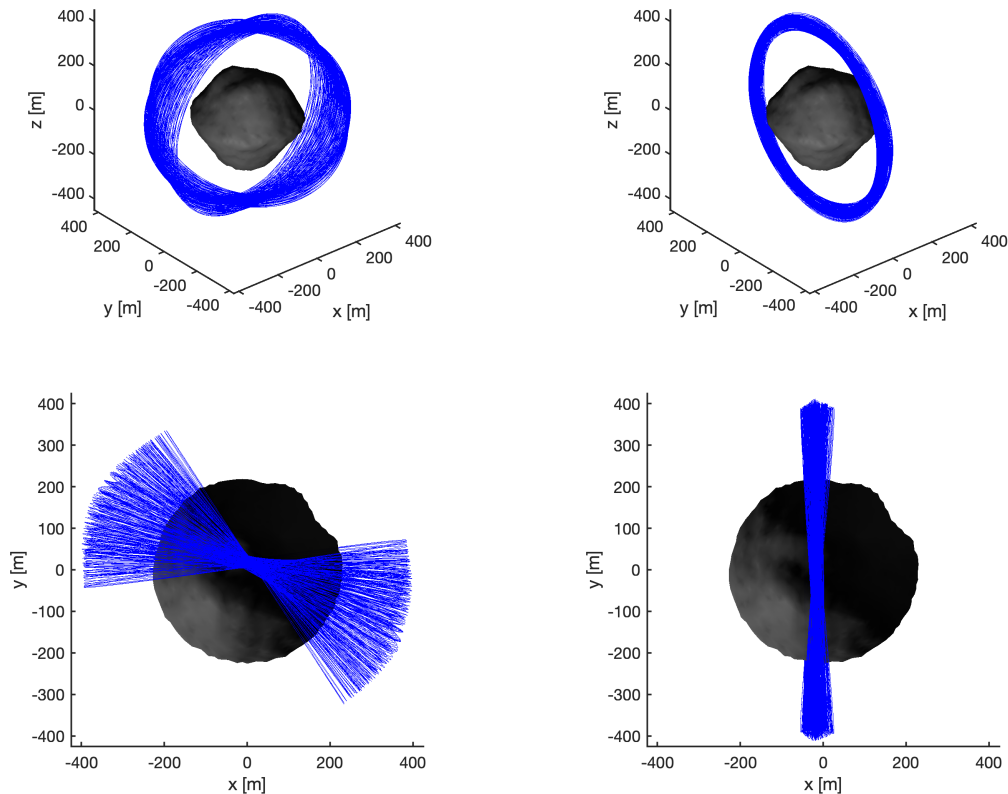
Figure 3: Nominal 400 m polar orbit around 2008 EV5. Spacecraft trajectory is shown in an inertial frame (left) and sun-synchronous rotating frame (right) viewed from a perspective angle (top) and from the asteroid pole (bottom).

The reason for this alignment is a combination of in-plane and out-of-plane effects of solar radiation pressure, as depicted through the orbits and forces shown in Figure 4. From left to right, the orbit is assumed to first be circular and aligned with the terminator with uniform gravitational force shown in red, and solar radiation shown in blue perpendicular to the orbit plane. The resulting torque over a full orbit is therefore close to zero, as shown by the vectors plotted at the asteroid center (Figure 4a). As the asteroid moves along its own orbit around the sun, the solar radiation pressure shifts in direction, resulting in energy injected into the upper half of the orbit and energy extracted from the lower half (Figure 4b). The effect of this work done on the orbit is a change in radius, with the lower half of the orbit raised and the upper half lowered. The increased time below the equatorial plane results in a torque applied by the solar radiation pressure to the orbital plane (Figure 4c), rotating the orbit plane so that the upper half is closer to the sun. This new misalignment of the solar radiation pressure causes further in-plane energy deposition during the leading half of the orbit and extraction during the trailing half (Figure 4d), resulting in orbit raising in the trailing half and orbit lowering in the leading half. Finally, the increased time in the trailing section of the orbit results in a torque about the vertical axis, rotating the orbit back into alignment with the sun direction.
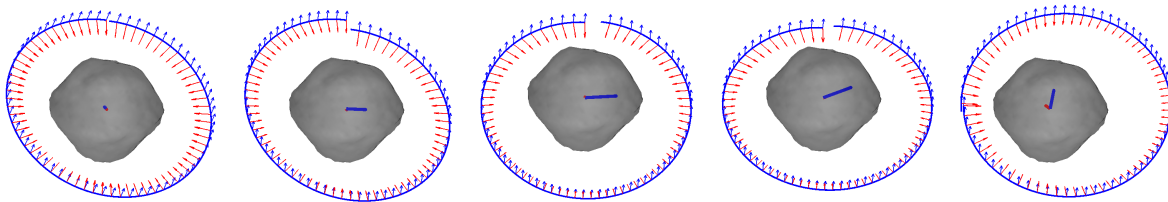
Figure 4: Snapshots of perturbed orbits close to a nominal circular 400 m illustrating the combination of effects that act on the orbit.

The individual effects outlined above are of course all active simultaneously, but the decomposition of the perturbations into individual in-plane and out-of-plane effects facilitates understanding of the way the orbits remain aligned with the sun direction and why they remain quasi-stable (bounded) but do not converge to a steady-state orbit.

3.2.1   Simulation framework

The orbital simulation for MIDEA was implemented in MATLAB, using a voxelized point-mass representation of 2008 EV5 similar to that used by *Llanos et al.* [2014] to capture the effects of asphericity and non-uniform asteroid density, and with solar radiation pressure modeled based on solar and asteroid positions during the proposed 2026 mission duration as predicted by the JPL HORIZONS system (available at ssd.jpl.nasa.gov/?horizons). The numerical integration of the equations of motion was performed in an inertial reference frame centered on the asteroidal center of mass and aligned with the asteroid's axis of rotation to simplify the physics and reduce the computational load. The rotation axis is assumed to be closely aligned with the orbital plane with a retrograde rotation period of 3.725 h [*Busch et al.*, 2011]. However, by basing the asteroid and

solar states on HORIZONS predictions, non-Keplerian effects result in minor perturbations to the orbital plane and deviations from perfectly elliptical orbits.

Figure 5 shows the trajectory of 2008 EV5 and the sun relative to the solar system barycenter for dates between 2020 Jan 1 and 2050 Jan 1, with the 50-day period after a targeted 2026 Aug 04 arrival highlighted in red. The non-Keplerian trajectory of the sun is clear over the thirty-year trajectory, though its position remains relatively constant over the duration of a short MIDEA mission regardless of start date.
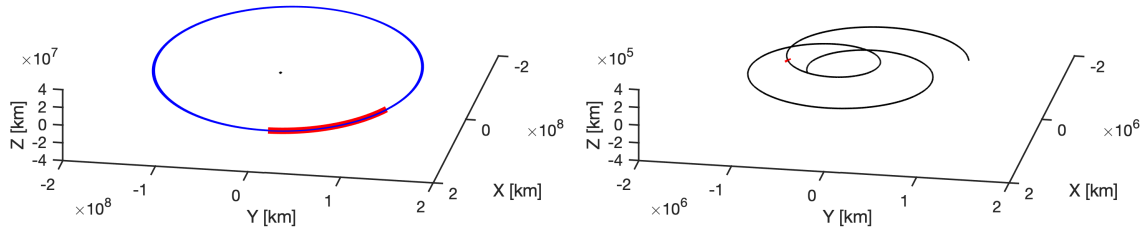
Figure 5: Trajectory of 2008 EV5 (left) and the sun (right) relative to the solar system barycenter from 2020 to 2050, with the targeted 50-day period in 2026 highlighted in red.

Figure 6 (left) shows a time history of the instantaneous orbital elements governing the orientation of the orbital plane over the thirty-year period. The inclination and longitude of ascending node are calculated daily, while the argument of periapsis is computed once per orbit by numerically determining the point of closest approach to the solar system barycenter. These values are tabulated and compiled into the histograms in Figure 6 (right). A reference frame is defined that is aligned with the mean of these values, corresponding to a mean inclination of 7.446 degrees, mean longitude of ascending node of 93.115 degrees, and mean argument of periapsis of 235.57 degrees. The standard deviations of these values are 0.0206, 0.222, and 3.26 degrees, respectively, from a sample set of 10959 orbital states and 31 passages of periapsis.
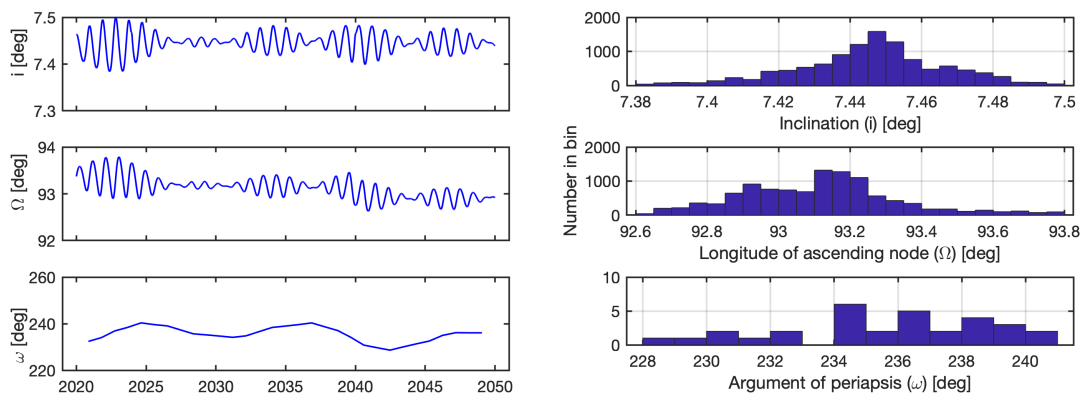
Figure 6: Time history (left) and histogram of instantaneous orbital elements describing the orientation of 2008 EV5's orbital plane relative to the solar system barycenter.

Solar radiation pressure was implemented in the model by implementing a lookup function that interpolates the HORIZONS data (obtained at 24 hour intervals) at each simulation time to calculate the instantaneous position of the sun and asteroid and their relative directions.

Figure 7 shows the results of a convergence analysis used to determine the MATLAB numerical integration tolerances best suited to simulate the MIDEA spacecraft trajectories. Twenty-two simulations were run using ode113 over a 50-day simulation time for a 250 g spacecraft orbiting a 10^{11} kg point-mass asteroid at a nominal orbit radius of 400 m, and subject to solar radiation pressure on 0.04 m^2 of frontal area. The initial conditions were specified to correspond to the ascending node positioned in the anti-ram direction with a circular orbit velocity in the positive z direction. These simulations used three values of relative tolerance (2.25×10^{-14}, 1×10^{-12}, and 1×10^{-10}) and seven values of absolute tolerance (10^{-10} to 10^{-22} in factors of 100), compared against a baseline case with relative tolerance of 2.25×10^{-14} and absolute tolerance of 10^{-24}. Figure 7 (left) shows the offset of each position trajectory compared to the baseline case, with the blue, green, and red traces corresponding to different levels of relative tolerance and the shading corresponding to absolute tolerance (lighter traces having a smaller value). The maximum value of each trace and the computation time for each simulation is summarized in the plots in Figure 7 (right). From these results, the most stringent relative tolerance value of 2.25×10^{-14} was selected, along with an absolute tolerance of 10^{-18} to provide a good balance between computation time and simulation accuracy.
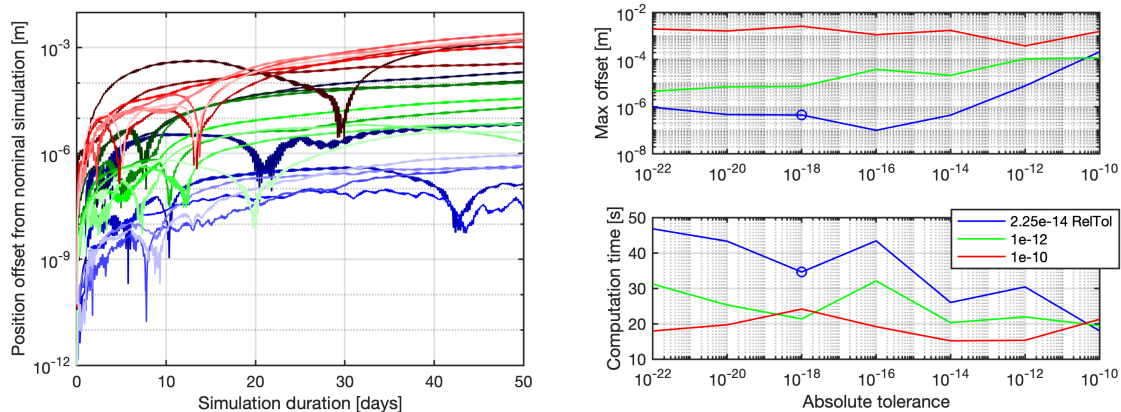
Figure 7: Time history of the relative offset of simulations over a range of absolute and relative tolerances (left) and their corresponding maximum offset and computation times (right).

A similar convergence analysis using a lighter spacecraft of 100 g demonstrated similar results, while comparison with ode45 and other integrators indicated that ode113 yielded better accuracy for a fixed computation time.

The shape model used to represent asteroid 2008 EV5 was obtained in .obj format based on observations using the Arecibo and Goldstone radars and the Very Long Baseline Array [*Busch et*

11

al., 2011]. Figure 8 shows the triangulated surface mesh composed 2000 vertices and 3996 facets, with an average facet area of 270 m².
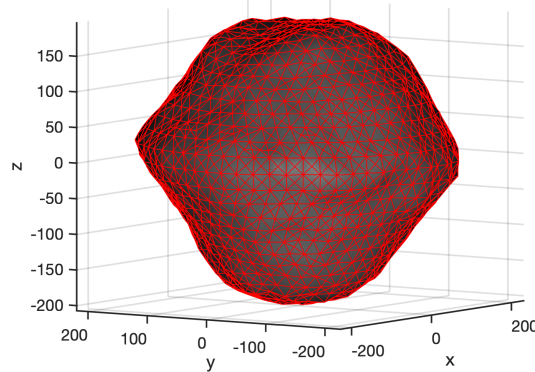
Figure 8: Shape model of asteroid 2008 EV5 with vertices and triangular faces shown in red.

To convert this surface mesh into a set of point masses representing the gravitational effect of the asteroid, a standalone function for mesh voxelization was obtained and used (www.mathworks.com/matlabcentral/fileexchange/27390-mesh-voxelisation). Unlike the voxel implementation used by *Llanos et al.* [2014], which was a radially symmetric set of 14,000 points, our representation of the asteroid was constructed using a cartesian grid and with sufficient resolution can capture surface asymmetries such as craters. Figure 9 shows the voxelization of the 2008 EV5 shape model at grid resolutions of 100 m, 50 m, and 25 m, consisting of 34, 280, and 2240 points, respectively. Additional models at resolutions of 10 m and 5 m with 34,202 and 276,079 points were constructed but are not shown here. The gravitational model was implemented only between the spacecraft and each point mass, with the set of asteroidal point masses rotating at a prescribed rate as a rigid body.
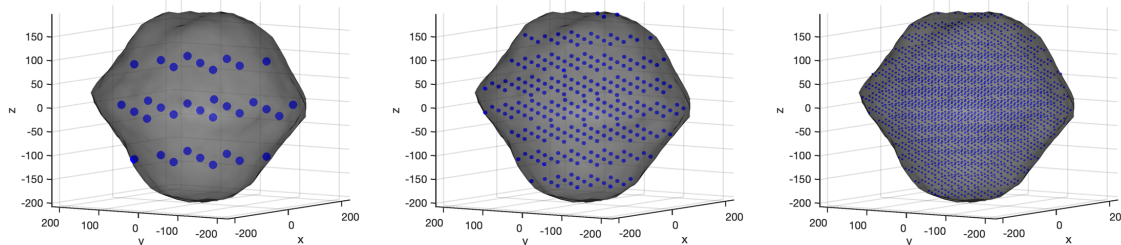
Figure 9: Voxel representation of asteroid 2008 EV5 at grid resolutions of 100 m (left), 50 m (middle), and 25 m (right).

Figure 10 shows the effect of voxel resolution on simulation trajectories using similar parameters to the convergence analysis above. Because of the substantially longer simulation times, this analysis was only simulated for 24 hours rather than 50 days. Figure 10 (left) shows the position offset of the coarser resolution simulations relative to the trajectory of the 5 m simulation, and Figure 10 (right) summarizes the number of voxels used and the corresponding

12

computation time. Based on the nearly 10x increase in computation time between the 25 m and 10 m cases, we decided to proceed with future simulations using the 25 m model despite the several meters of offset shown over the 24-hour simulation.
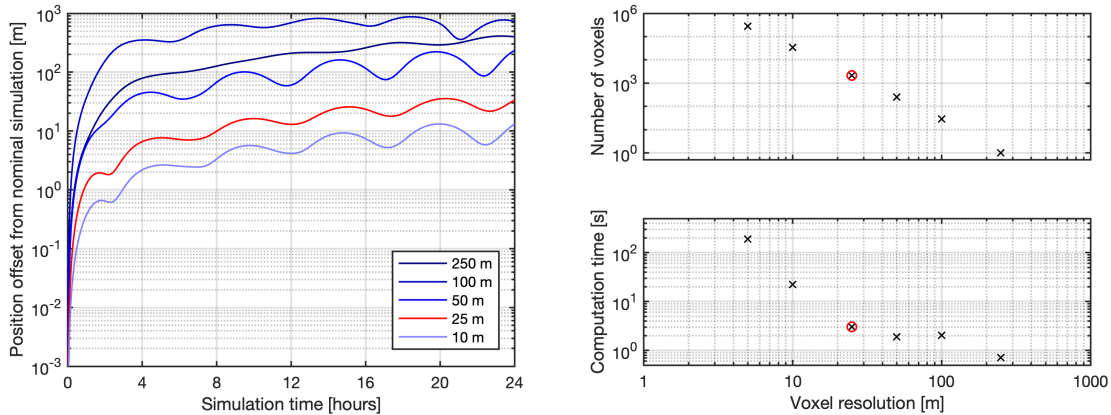

Figure 10: Time history of the relative offset of simulations over a range of asteroid voxel resolutions (left) and their corresponding maximum offset and computation times (right). The selected 25 m resolution is highlighted in red.

3.2.2 Numerical results

With the simulation framework and parameters identified above, we conducted a study of the orbital parameters relevant to the design of the MIDEA sensor constellation, considering robustness to uncertainties in asteroid mass, sensitivity to initial conditions, and effect of orbit size. A survey of arbitrary initial conditions in this simulation demonstrated escape or collision in less than a day, rendering most orbit families infeasible for the expected 20- to 50-day MIDEA mission. The polar terminator orbit was therefore identified as the primary candidate solution.

Asteroid 2008 EV5's total mass remains highly uncertain and is reported to be $(1.0 \pm 0.5) \times 10^{11}$ kg [*Busch et al.*, 2011]. Because of the large area-to-mass ratio of the free-flying sensors, they consequently experience substantial orbital perturbation resulting from solar radiation pressure and risk being ejected from the asteroid's sphere of influence into heliocentric orbit. Figure 11 shows one-day simulations of 100 g and 150 g spacecraft orbiting 2008 EV5 over a range of asteroid masses from 4×10^{10} kg to 1.6×10^{11} kg at intervals of 2×10^{10} kg. For both of these cases, the spacecraft is unable to maintain orbit around the lowest mass asteroids (corresponding to the darkest traces) and is quickly ejected. Figure 12 shows the same simulation conditions for a spacecraft mass of 250 g, with the spacecraft remaining in orbit around 2008 EV5 under all asteroid mass conditions. The mass of the plasma sensor spacecraft was therefore increased to 250 g from the initial design target of 50–100 g, in order to be robust to the uncertainty in asteroid mass.

13
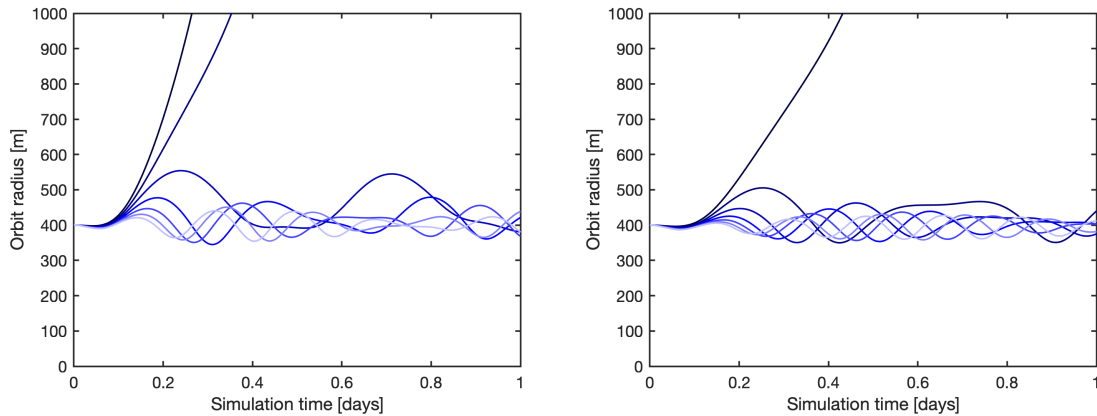
Figure 11: Simulated trajectories of a 100 g (left) and 150 g (right) spacecraft around asteroid 2008 EV5 over a range of asteroid masses from 4×10^{10} kg to 1.6×10^{11} kg showing unstable trajectories for the lowest-mass cases in dark blue.
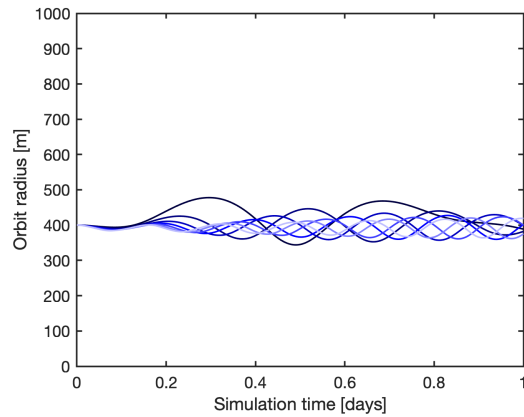
Figure 12: Simulated trajectories of a 250 g spacecraft around asteroid 2008 EV5 over a range of asteroid masses showing bounded orbits for all asteroid mass cases.

To identify the optimal orbit radius for the MIDEA spacecraft, simulations were run with initial radii ranging from 300 m to 1000 m at intervals of 25 m, assuming a rotating 1.0×10^{11} kg asteroid voxelized using a 25 m grid resolution. All trajectories starting at a radius of 750 m and above escaped from the asteroid within the duration of the 50-day simulation. Selected trajectories between 300 m and 700 m are shown in Figure 13 in the rotating sun-synchronous frame. The smallest orbits are highly perturbed by the aspherical gravitational field of the asteroid, while the larger orbits are more greatly perturbed by solar radiation pressure.

Figure 14 (left) shows selected time histories of the orbit radius from initial conditions between 300 m and 700 m showing that the higher orbits are immediately highly variable while the 300 m orbit is initially well behaved with a variation that grows over time. Figure 14 (right) summarizes the variation in these orbital trajectories, with the top plot showing the extent that the orbital radius varies over the simulation, and the lower figure showing the variation in the cross-track (out-of-

14

plane) direction. These simulations show that orbits at around 400 m radius remained the most consistent over time.
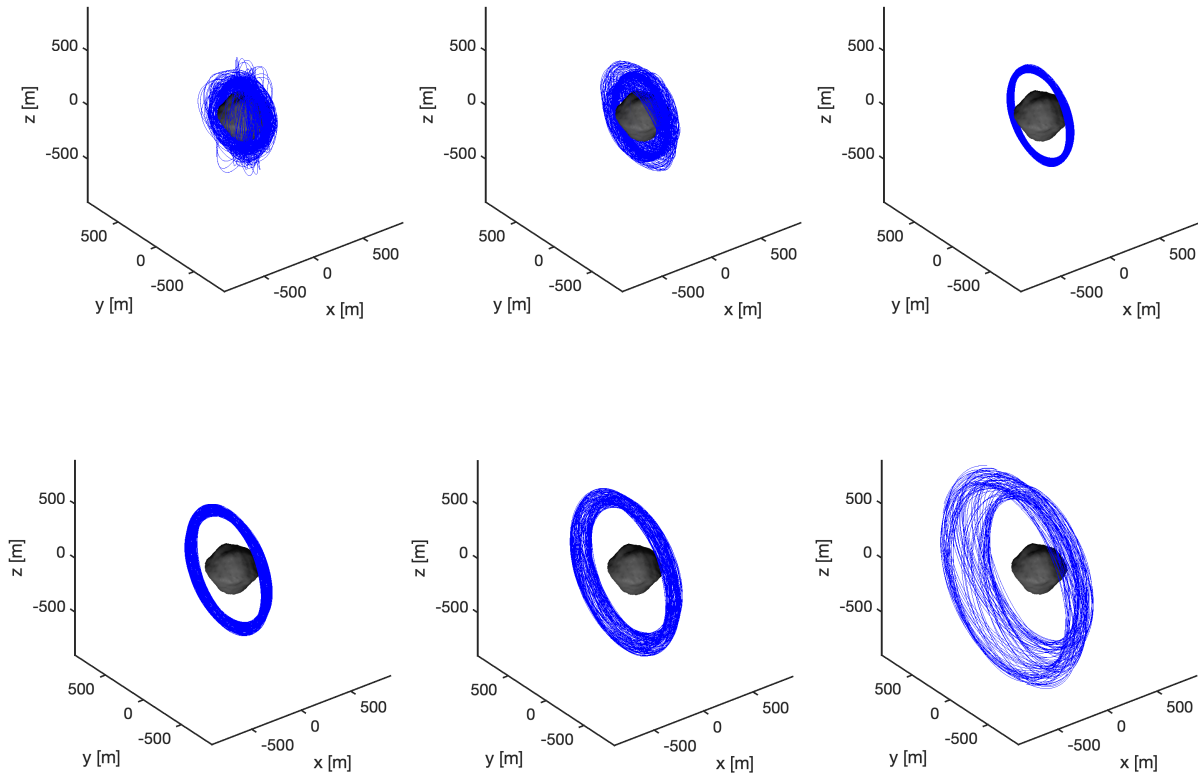
Figure 13: Spacecraft orbit trajectories in the sun-synchronous rotating frame with nominal radius of 300 m (top left), 350 m (top middle), 400 m (top right), 500 m (bottom left), 600 m (bottom middle), and 700 m (bottom right).
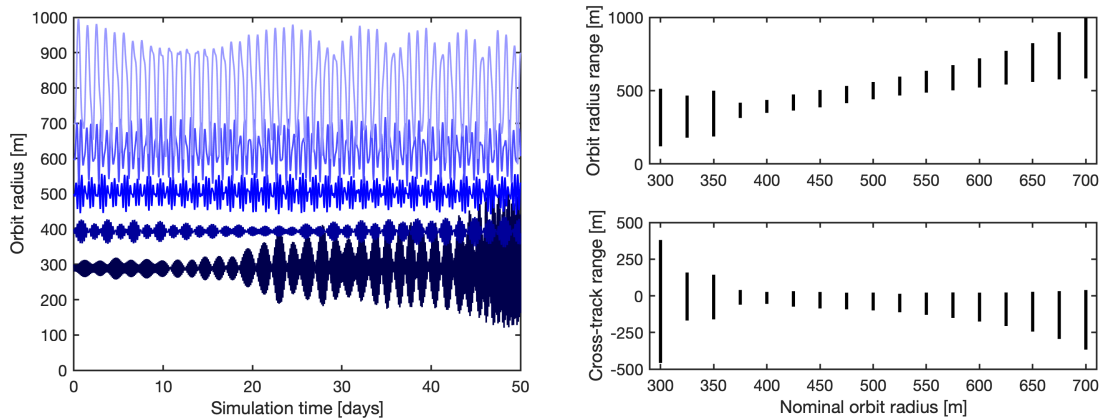
Figure 14: Time history of orbit radius over a 50-day simulation for five cases spanning 300 m to 700 m nominal orbit radius (left), and the total range in the radial and cross-track directions for 17 cases at intervals of 25 m in nominal orbit radius (right).

15

For the initial velocity perturbations, simulations were run using the same 1.0×10^{11} kg asteroid model with a 400 m nominal orbital radius, for which the circular velocity is 12.9 cm/s and the orbital period is 5.4 hours. Perturbations in the initial velocity were introduced with values of 0.1, 0.2, 0.5, 1.0, 1.5, and 2.0 cm/s positive and negative, in the along-track and cross-track directions. Figure 15 summarizes the results of these simulations in terms of the variation in orbital radius and in the cross-track direction; the red lines correspond to orbits with an initial perturbation in the along-track velocity, while the blue lines indicate an initial cross-track perturbation in velocity. This result emphasizes the highly sensitive nature of asteroid proximity operations: a deployment uncertainty of millimeters per second can result in the potential loss of a sensor from the constellation.
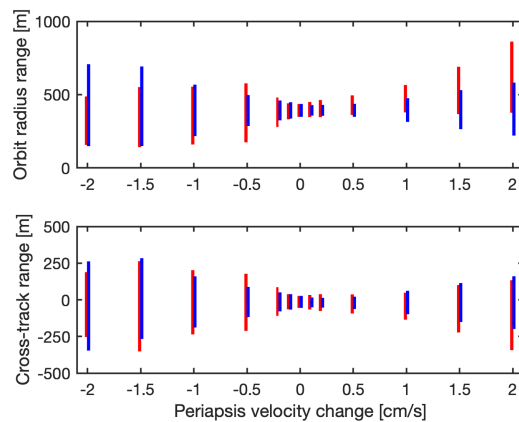
Figure 15: Orbital perturbations as a function of initial velocity over a range of ±2 cm/s with velocity perturbations in the along-track (red) and cross-track (blue) directions.

An advantage of the voxel representation used in these orbital simulations is the ability to make local modifications to the gravitational environment to study their effect on orbit stability. To this end, we introduced two mass concentration configurations as illustrated in Figure 16. The first configuration (Figure 16, top) removed mass from two locations at $[100, 100, 0]^T$ and $[-100, -100, 0]^T$ by introducing additional negative point masses at those locations, and addition an equivalent mass at $[100, -100, 0]^T$ and $[-100, 100, 0]^T$. These symmetric locations were selected to avoid shifting the principal axis of inertia of the asteroid. The second configuration (Figure 16, bottom) removed mass from the same location but introduced the additional mass at $[150, -150, 0]^T$ and $[-150, 150, 0]^T$ to represent a shallower mass concentration. Simulations were run with the value of each removed and added point mass ranging logarithmically from 1 kg to 10^9 kg (1% of the total asteroid mass). Figure 17 summarizes the results of these simulations, showing little effect from all but the largest mass concentrations, but a slightly greater effect from the shallower configuration.
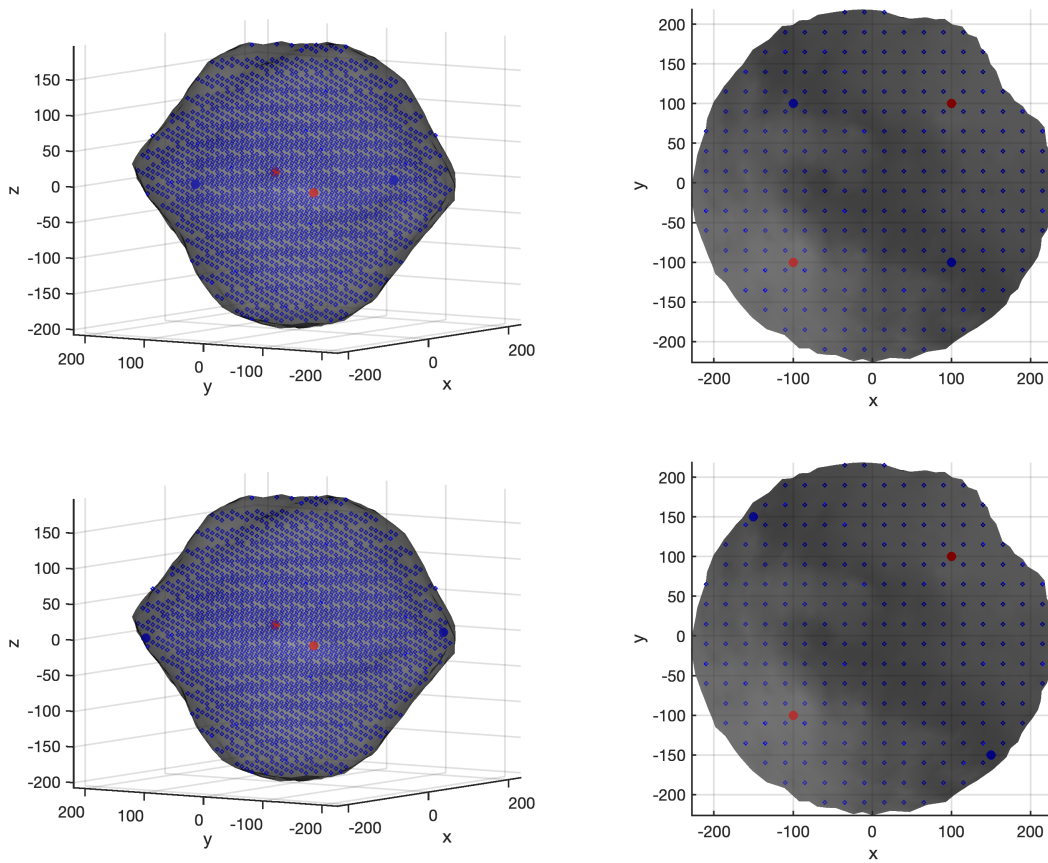
Figure 16: Two asteroid configurations used to determine the effect of mass concentrations on orbit perturbations, with mass removed from the locations marked in red and added to the locations marked in blue, while maintaining reasonable inertia properties corresponding to the asteroid's rotation.
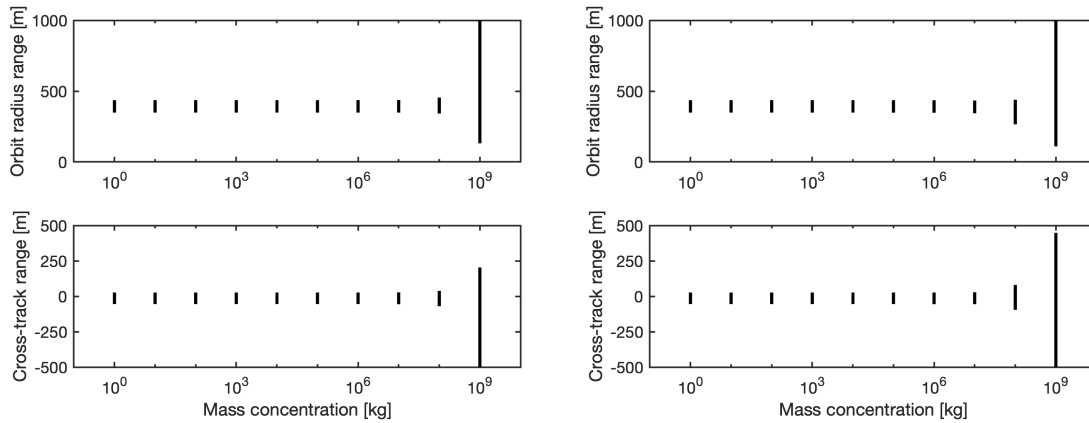
Figure 17: Orbital perturbations over a range of mass perturbations corresponding to configuration 1 (left) and configuration 2 (right) showing little effect below 10^8 kg and with greater effect from shallower mass concentrations.

To summarize, the optimal orbit selected for the MIDEA constellation assuming a 10^{11} kg asteroid is a circular 400 m polar orbit corresponding to an orbital period of approximately

5.4 hours, requiring an insertion velocity precision of 5 mm/s or better. Because of the high sensitivity of the orbital conditions to total asteroid mass, a likely deployment scenario would involve initial preliminary gravitational characterization through proximity operations just involving the mothership spacecraft before deploying the more sensitive plasma sensors, and adjusting the operational orbit radius or possibly adjusting the sensor spacecraft mass using ballast.

3.3   Plasma sensor design

The initial concept for the ultralight plasma sensor spacecraft was a 100 g planar structure composed of a central panel containing the sensor electrode and spacecraft bus electronics, surrounded by four foldout solar panels using optical concentrators to minimize the mass of the required photovoltaic cells and cover glass. However, the polar orbit identified in Section 3.2 necessitates two major changes: the spacecraft mass was increased to 250 g and the solar panels must be perpendicular to the plasma sensor electrode to allow the spacecraft to simultaneously generate power and provide observations of impact plasma from the asteroid surface. In this section, a revised plasma sensor design is proposed to accommodate these changes, and a preliminary concept for attitude control and localization is developed.

3.3.1   Mechanical configuration

With the selection of a polar terminator orbit for the sensor constellation, the asteroid surface (nadir) will always be perpendicular to the sun direction. Additionally, for the spacecraft to be dynamically stable, its principal axis corresponding to the greatest moment of inertia must be aligned with the orbit normal. Figure 18 shows a proposed geometric configuration that can be folded flat into a 10×10 cm package for stowage in the mothership. This configuration also allows for the solar panels to be exposed before they are unfolded, enabling power generation immediately upon deployment.
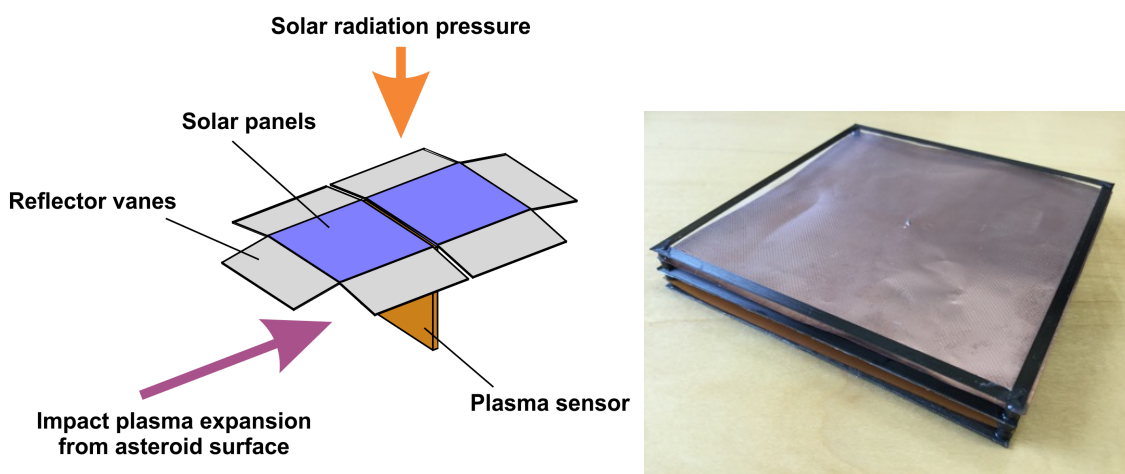
Figure 18: Sensor spacecraft configuration showing two solar panels in blue, the plasma sensor in orange, and reflector vanes in grey (left), and plasma sensor prototype fabricated for the ESI project (right).

Using this geometry, the mass of the spacecraft should be distributed primarily within the solar panels rather than the perpendicular plasma sensor in order to maintain favorable inertia properties. Allocating 100 g to each of the solar panels, 5 g to each of the six reflector vanes, and 20 g to the plasma sensor results in moments of inertia of 0.00126, 0.00103, and 0.00035 kg m^2, with the greatest moment of inertia aligned with the solar panel normal. This mass allocation allows for a 21% margin in the greatest moment of inertia over the intermediate axis.

The 20 g mass allocated to the plasma sensor offers substantial margin compared to the prototype fabricated for the ESI project (Figure 18, right). This prototype was fabricated using a pultruded carbon fiber frame with sensor electronics mounted on a flexible printed circuit board (PCB). The mass of the unpopulated flex PCB was determined to be 980 mg, with the populated PCB coming to 1042 mg. In comparison, a conventional rigid PCB using FR4 would be 20 to 40 grams, depending on thickness and copper weight. Incorporating additional layers of copper-clad Kapton for the collector electrode and high transparency stainless steel grids for electrical shielding, the final mass of this prototype stack (not including the deployable solar concentrators or electronics for the spacecraft bus) was 6.86 g.

Allocating 100 g to each solar panel allows for the use of conventional FR4 PCBs and solar cells to enhance the rigidity of the overall structure and avoid the complexity and stringent pointing requirements associated with solar concentrators. The spacecraft bus electronics can easily be integrated on the back side of these PCBs using a design similar to the Sprite chipsat [*Manchester et al.*, 2013], which fits on two sides of a 4 × 4 cm PCB including solar cells.

The six reflector vanes are each 5 × 10 cm and includes additional area for solar power generation as well as controlled reflectivity devices for attitude control. Perovskite-based solar cells [*Eperon et al.*, 2016; *Bush et al.*, 2017] show promise as a lightweight alternative for space-based power generation, and could be applicable to increasing the solar collecting area while reducing the total mass of photovoltaic material and cover glass required to provide sufficient power. These vanes are each canted at 10 degrees from the plane of the solar panels to provide a passive restoring torque when the spacecraft attitude is perturbed from its nominal sun-pointing orientation. We considered several alternative technologies for implementing active attitude control, including LCDs to adjust the reflectivity of the surface as well as actuated mechanisms for changing the reflector angle or the spacecraft center of mass. From these options, controlled reflectivity using LCDs was selected as the most attractive option. Actuated mechanisms require bulky and massive motors, or piezo actuators that operate through repeated cycling over amplitudes of up to 100 V, which would be a substantial power draw. Additionally, these mechanical options would not necessarily reset to a balanced configuration if power is lost, while the LCD option would naturally restore its symmetric state. Controlled reflectivity devices implemented using polymer dispersed liquid crystals have been demonstrated on the IKAROS solar sailing spacecraft [*Saiki et al.*, 2012]. In contrast to the piezo devices considered, they only require voltage boosts up to approximately 40 V to operate [*Sheraw et al.*, 2002] and can be as thin as 150 μm [*Chujo et al.*, 2018], yielding a contrast ratio of up to 10^3 [*Mach et al.*, 2001].

3.3.2   Attitude control

The efficacy of the reflectivity control scheme was assessed by implementing a 2D attitude control simulation in MATLAB representing rotation about the two minor principal axes. Torques in these directions can be actuated by differentially switching the LCDs on opposite sides of the spacecraft, while a torque can be actuated about the major principal axis by switching the diagonally opposite LCDs. By reducing the reflectivity of one side of the spacecraft, the equilibrium orientation can be adjusted. In this simulation, we decompose the effect of solar radiation pressure on each reflector vane into an absorption and emission component, and switch the coefficient of emission from 0.8 to 0.5 when the LCD is actuated. Results are presented here for dynamics about the intermediate axis, which has a slower response than the axis about the least moment of inertia.

In Figure 19, two sets of oscillatory and undamped phase portraits are shown, corresponding to the left and right LCDs being independently actuated. The unbalanced reflectivity results in the equilibrium orientation shifting by approximately three degrees. Between these two states, a switching line control law can be defined, which only requires a measurement of the sun angle and its time rate of change. The line shown in magenta separates regions in state space where one or the other LCD is actuated.
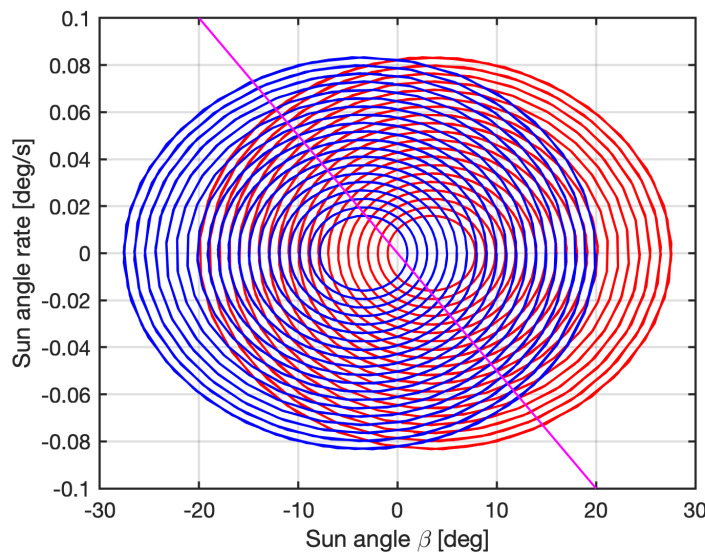
Figure 19: Phase portrait of the two biased reflectivity conditions, in red and blue, with the switching line indicated in magenta.

A simulation of these rotational dynamics using a switching line slope of 0.01 results in the trajectories shown in Figure 20 from a range of initial pointing offsets up to 60 degrees. The time histories in Figure 20 (left) indicate that the natural frequency of these dynamics is under 50 minutes, which is substantially shorter than the 5.4 h orbital period. Using the switching line control law introduces a damping effect that settles the largest offset within about two hours. From the phase portrait in Figure 20 (right), these dynamics encapsulate rotation rates up to 0.1 degrees

per second, though more extreme initial conditions also were shown to eventually stabilize in simulation results not included here.
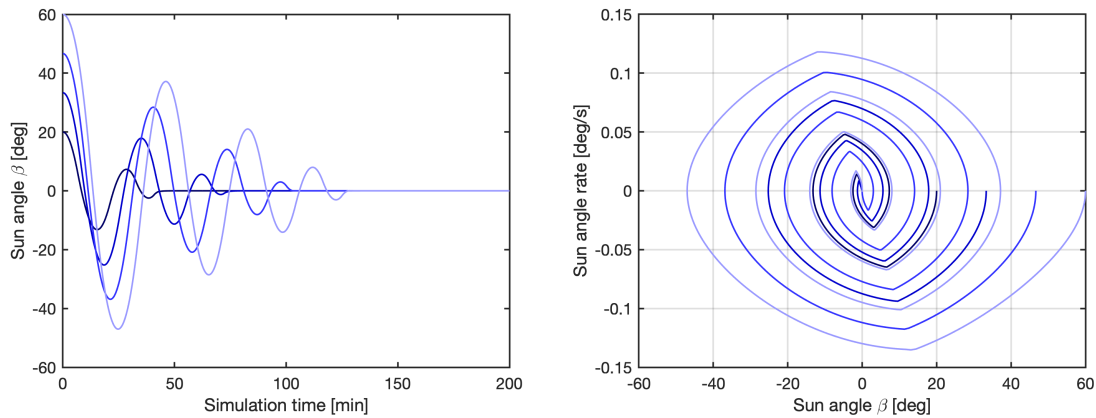
Figure 20: Time history (left) and phase portrait (right) of the spacecraft attitude over a range of initial pointing offsets ranging from 20 to 60 degrees.

These results demonstrate promise in the proposed sensor mechanical design and attitude control strategy using controlled reflectivity devices with flight heritage. The simple switching line control law provides rapid regulation of perturbations from the sun-pointing orientation, and can be supplemented with a more complex 3D control law to provide control over orbit modifications needed to maintain the formation of the MIDEA constellation.

3.3.3   Constellation localization

One critical aspect of a system for maintaining the geometry of the MIDEA constellation and identifying the point of origin of any detected impact plasma is the need to localize each sensor relative to the asteroid surface. Initial concepts for the implementation of a system to determine the position of each sensor included directional RF ranging and possibly optical tracking from the mothership. However, with the increased mass margin of the sensor spacecraft, it is possible to include a camera on each in order to aid in navigation and position determination.

As a proof of concept demonstrating the capabilities of optical-only navigation using off-the-shelf techniques, we took advantage of the recent arrival of the OSIRIS-REx spacecraft at asteroid Bennu to provide representative images similar to what would be seen from a spacecraft around 2008 EV5. Bennu is a 492 m carbonaceous asteroid in a 1.1264 AU Earth-crossing orbit and is roughly spherical with an equatorial bulge, similar to the geometry of 2008 EV5. The OSIRIS-REx spacecraft arrived at Bennu on 2018 Dec 3 and obtained a sequence of images of the asteroid from a distance of 80 km using its PolyCam instrument. This sequence of 36 images was compiled into an animated .gif file in the public domain on Wikimedia Commons (located at commons.wikimedia.org/wiki/File:Asteroid-Bennu-OSIRIS-RExArrival-GifAnimation-20181203.gif). We extracted the 36 individual image frames as 900×900 pixel .jpg files, four of which are shown in Figure 21.
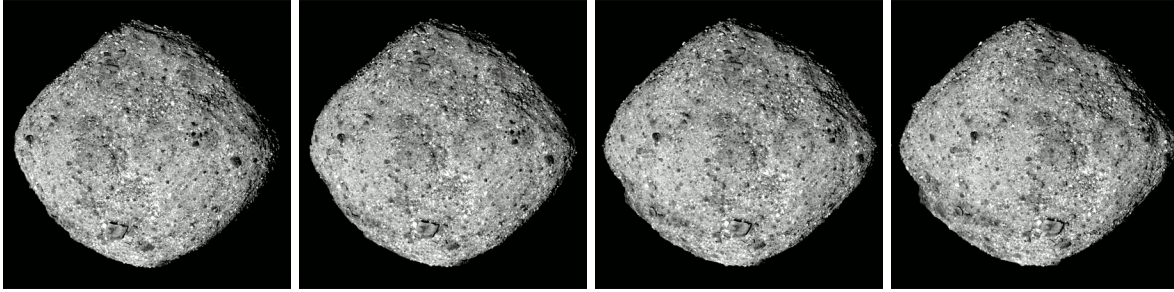
Figure 21: Public domain images of asteroid Bennu as seen by the PolyCam instrument on OSIRIS-REx from a distance of approximately 80 km (NASA/Goddard/University of Arizona).

These images were used as the input in a VisualSFM workflow [*Wu*, 2013], which identifies scale-invariant feature transform (SIFT) keypoints in the image sequence as shown in Figure 22, identifies corresponding features between image pairs, and implements a structure from motion (SFM) and bundle adjustment algorithm to compute an estimate of the 3D locations of corresponding SIFT features and camera locations. Figure 23 shows the number of corresponding SIFT features identified between pairs of images. The VisualSFM software found about 15000 features from each image; about 2000–3500 matches were found between adjacent images, 500–1300 between images separated by one, dropping to about 10–20 spurious matches between pairs that should not share any common points.
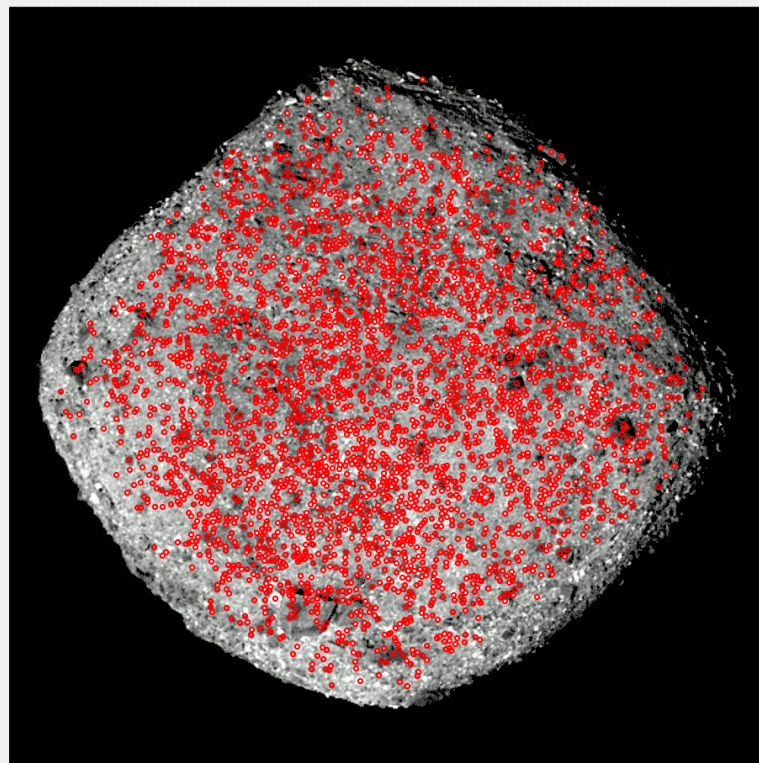
Figure 22: SIFT features identified on one image of asteroid Bennu.
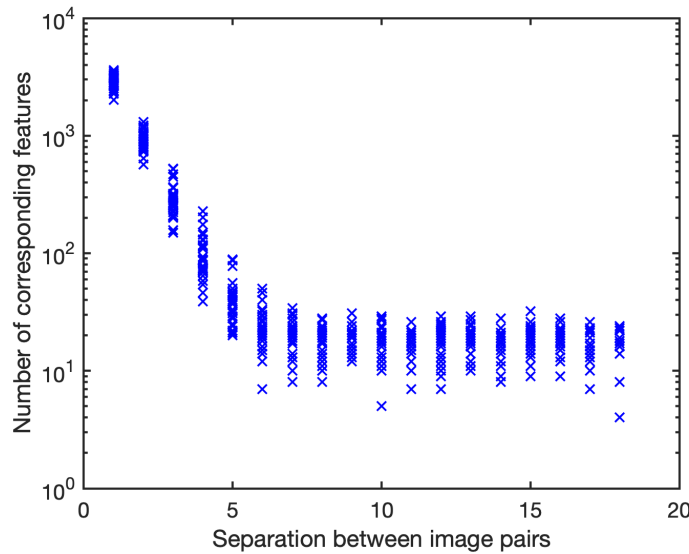
Figure 23: Number of corresponding SIFT features between frames, showing a high number of corresponding pairs between adjacent images and a low baseline number of false correspondences.

VisualSFM ran its standard 3D reconstruction algorithm with no knowledge of the camera locations, producing the output depicted in Figure 24. Since the source images were obtained from the asteroid spinning relative to the spacecraft, the algorithm should ideally have determined all cameras to be at constant radius. The results for camera position did not successfully capture this constant radius well, but was relatively accurate in determining the relative orientation of the camera from the asteroid surface. With the inclusion of dynamic constraints from knowledge of the spacecraft motion, this off-the-shelf algorithm could be easily modified to produce more accurate results.
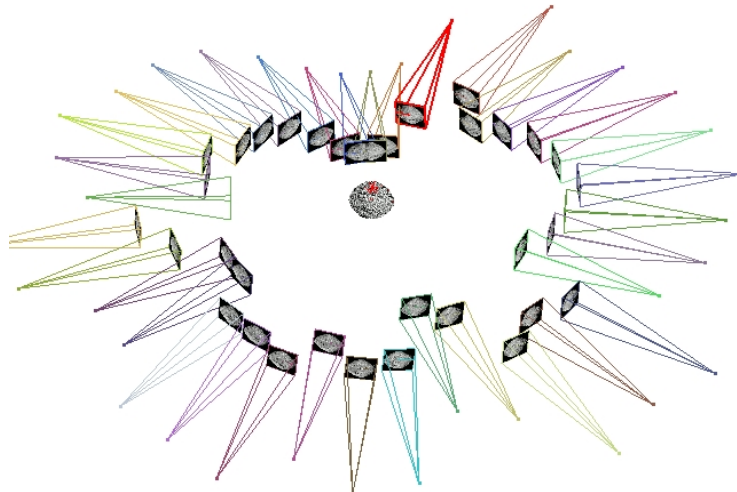
Figure 24: 3D reconstruction of the asteroid geometry and estimated relative positions of the camera with no dynamic constraints.

Figure 25 shows the final output of the dense 3D reconstruction algorithm, showing some sparsity in the polar regions that were not well captured in the image sequence, but capturing notable surface features including a large boulder in the southern hemisphere.
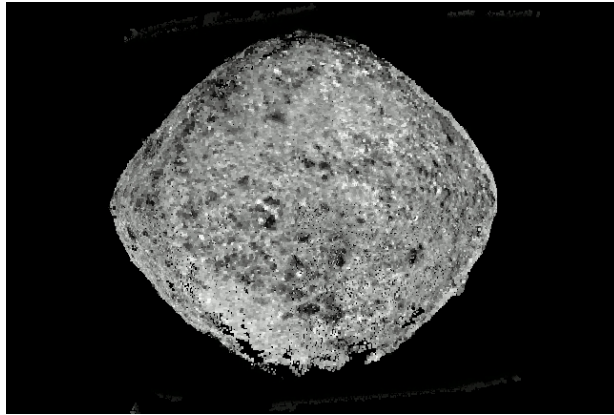
Figure 25: Image of asteroid Bennu extracted from the 3D model reconstructed using the above image sequence.

4   Plasma detection rate and mission duration

The underlying principle of MIDEA is to take advantage of meteoroid impacts on asteroids to liberate material from the asteroid surface such that it can be detected by an orbiting constellation of sensors. Meteoroids are present throughout the solar system and can impact other bodies such as spacecraft and asteroids at tens of kilometers per second [*Grün et al.*, 1985; *Drolshagen*, 2009].

When a meteoroid impacts an asteroid surface, the relative speed is typically several times the speed of sound in the material, such that the inertial stresses are dominant over material strength. This type of impact is known as a *hypervelocity impact*, and results in vaporization and ionization of material from the impact surface and from the impacting meteoroid. The resulting plasma is initially extremely dense, and rapidly expands under the influence of the internal plasma dynamics and driving forces from the external environment. Time-of-flight mass spectroscopy has been used to determine the composition of hypervelocity impact plasmas in the laboratory environment [*Ratcliff et al.*, 1997; *Lee et al.*, 2013] and in space [*Srama et al.*, 2004]. The MIDEA concept extends this principle by using the asteroid surface as the impact target and measuring the time of flight of ions over a distance of 100–300 m to the spacecraft.

4.1   Hypervelocity impact plasma

The material excavated from an asteroid surface by a meteoroid impact includes solid and molten ejecta, but some of this material is vaporized and ionized, forming a plasma that expands into the environment around the asteroid [*Dietzel et al.*, 1972; *Crawford and Schultz*, 1999; *Burchell et al.*, 1996; *Lee et al.*, 2013]. The initially dense plasma expands rapidly, subject to the electrical charge conditions of the surface. If the surface is in sunlight, it will be positively charged due to the photoemission of electrons, and will therefore attract the electrons and repel positive

ions [*Zimmerman et al.*, 2014]. In this section, we discuss the quantity of plasma produced in an impact event and the behavior of the plasma as it expands outward from the asteroid surface.
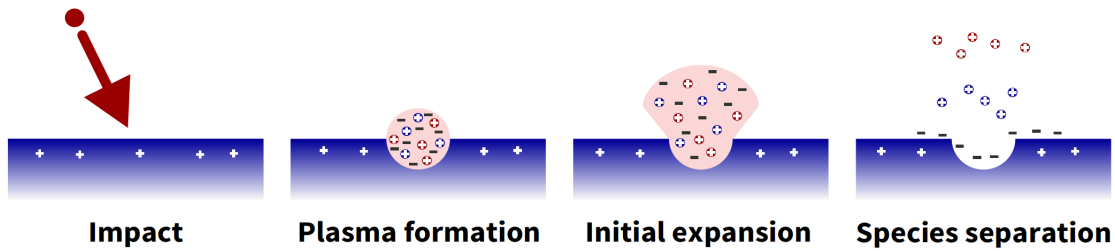
Figure 26: Depiction of processes involved in hypervelocity impact plasma formation and evolution.

4.1.1   Impact plasma production

Plasma production from meteoroid impacts has been studied extensively in ground-based hypervelocity impact experiments using dust accelerators [*Friichtenicht*, 1962; *Auer et al.*, 1968; *Lee et al.*, 2012; *Close et al.*, 2013], as well as through theoretical models [*Drapatz and Michel*, 1974] and numerical simulations [*Fletcher and Close*, 2014; *Song et al.*, 2013]. Based on empirical measurements, the charge produced by an impact can be represented as a power law depending on the meteoroid mass or size and the impact speed, given by

$$q = Cm^{\alpha}v^{\beta}, \tag{1}$$

where *m* is the impactor mass, *v* is the impact speed, and *C* is an experimental constant that depends on the material of the impactor and target. The mass exponent α is typically close to 1 and the speed exponent β has been reported with values ranging from 2.7 to 4.74 [*Dietzel et al.*, 1973; *Ratcliff et al.*, 1997] depending on the experiment. Note that the charge produced is nearly proportional to the meteoroid mass, but is much more strongly dependent on impact speed. In Figure 27, we plot the impact plasma produced as a function of impact speed and normalized by impactor mass for a selection of representative experiments from the literature, including the following:

- *Dietzel et al.* [1972] used a Van de Graaff dust accelerator to impact iron dust particles ranging from 1×10^{-15} to 5×10^{-10} g on tungsten targets at 0.2–40 km/s.
- *Burchell et al.* [1996] used a Van de Graaff dust accelerator to impact iron dust particles ranging from 2×10^{-16} to 3×10^{-11} g on molybdenum and ice targets at 2–60 km/s.
- *Crawford and Schultz* [1999] used a light gas gun to impact 0.32–0.64 cm aluminum projectiles into a powdered carbonate (dolomite) target at 0.8–7 km/s.
- *McBride and McDonnell* [1999] used results from accelerator tests for the calibration of cosmic dust detectors.

Note that, although the trends are mostly similar, the amount of plasma produced varies by over two orders of magnitude.
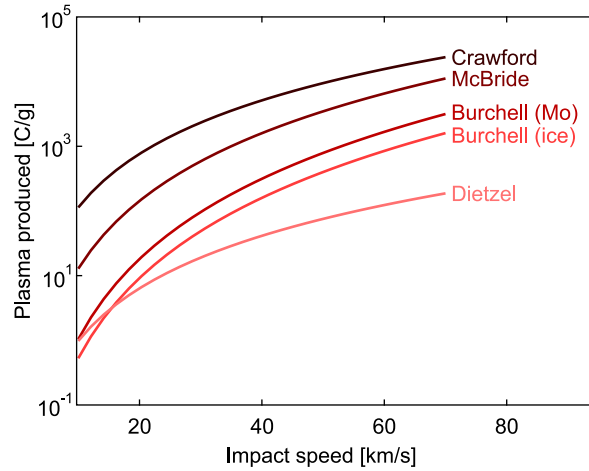
Figure 27: Impact plasma produced in coulombs per gram of impactor as a function of impact speed, based on prior ground-based experiments.

As the plasma is initially formed, it occupies a space similar to the size of the excavated crater. Crater formation from hypervelocity impacts has also been studied in literature, resulting in empirical relations such as

$$p = k m^{0.352} \rho^{0.167} v^{0.667},$$
(2)

where p is the penetration depth in cm, k is an empirically determined target material constant (0.42 for aluminum alloys and 0.25 for stainless steel), m and ρ are the meteoroid's mass in g and density in g cm^{-3}, respectively, and v is again the impact speed in km/s [*Frost*, 1970]. Alternatively, *Melosh* [1989] presents a pi-group approach to dimensional analysis in order to obtain a scaling law for impact crater formation. This analysis yields a power law for cratering efficiency that can be written as

$$V_c = C_V \frac{m_p}{\rho_t} \left(\frac{1.61 g d_p}{v^2} \right)^{-\xi},$$
(3)

where V_c is the crater volume, ρ_t is the impact surface density, g is the gravitational acceleration, and C_V and ξ are experimentally determined constants.

From these relations, a 1 ng meteoroid with a density of 3 g/cm^3 (approximately 10 microns) impacting at 20 km/s would produce a charge of 10^{-8} C, which would be detectable above the background solar wind plasma density at a distance of several hundred meters. From the volume ratio of the meteoroid and crater, the plasma is estimated to be at least 98% composed of material from the asteroid and the remainder from the impacting meteoroid. This is consistent with numerical simulations [*Fletcher et al.*, 2015].

4.1.2   Impact plasma expansion

The initial expansion of this dense plasma is complicated and not fully understood, but eventually the density drops to where Debye shielding breaks down and external electric fields can

26

penetrate into the bulk of the plasma, causing electrostatic acceleration and separation of oppositely charged species. In the case of impact plasmas occurring in deep space, the interplanetary magnetic field B (approximately 7 nT at 1 AU [*Kivelson and Russell*, 1995]) is small enough that the ion Larmor radius is typically on the order of kilometers and can be neglected for particle motion on the scale of hundreds of meters. As a limiting case, a singly charged hydrogen atom traveling perpendicular to the field at 2 km/s has a Larmor radius of 3 km, resulting in less than 2 degrees of deflection over 100 m of travel or a 0.005% change in the time of flight. Heavier and faster ions will have correspondingly larger Larmor radii.

In order to determine the composition of the asteroid surface, we seek impact events where the surface is positively charged, such that electrons are re-absorbed and positive ions are ejected into space. The detectability of the impact depends on the geometry of the plume of ejected ions: a narrower plume would produce a stronger signal over a greater distance, but only in the direction of the plume.

We model the plume angle to be equivalent to the final trajectory of an ion that is initially at the edge of the impact plasma [*Lee et al.*, 2017]. Its velocity can be decomposed into a component parallel to the asteroid surface and one that is normal. We assume that the parallel component is imparted by electrostatic repulsion from the remaining ion population. If the potential energy of a singly charged ion on the edge of a sphere of radius R_0 and charge Q is converted into kinetic energy, the final velocity is

$$v_\parallel = \frac{2}{m_i}\sqrt{\frac{k_e q_e Q}{R_0}},$$

(4)

where m_i is the ion mass, k_e is the electrostatic constant, and q_e is the elementary charge. We assume that the perpendicular component has contributions from an initial bulk velocity as well as repulsion from the positively charged surface, giving

$$v_\perp = v_{bulk} + \frac{2}{m_i}\sqrt{q_e V_s}.$$

(5)

Combining these two terms yields the plume angle

$$\theta_{plume} = \tan^{-1}\left(\frac{v_\parallel}{v_\perp}\right).$$

(6)

The surface potential of an asteroid is estimated to reach approximately 4 V in sunlight [*Zimmerman et al.*, 2014], and the bulk velocity of the expanding impact plasma has been found through simulation to be approximately 20 km/s [*Fletcher et al.*, 2015]. A remaining unknown quantity is the initial radius R_0 at which the electrons have been re-absorbed. While the dynamics of electron depletion from the plasma plume is the subject of further study through simulation and experiments, we can obtain order-of-magnitude bounds using two approximations.

First, through double layer theory [*Block*, 1978], the electron saturation current is derived from the Bohm condition as

$$j_{e,\text{max}} = q_e n_e \sqrt{k_B \left(\gamma_e T_e + T_i\right)/m_e}.$$

(7)

If we assume that this saturation current is drawn out out of the plasma until electrons are completely absorbed, this yields the differential equation

$$r^3 \dot{n}_e q_e = -r^2 j_{e,\text{max}},$$

(8)

which can be rewritten as

$$\dot{n}_e = \left(\frac{-\sqrt{k_B \left(\gamma_e T_e + T_i\right)/m_e}}{v_{\text{bulk}}}\right)\frac{n_e}{t} = C_1 \frac{n_e}{t},$$

(9)

assuming that the plasma initially expands at the bulk velocity v_{bulk} starting from an initial time $t_0 > 0$. The analytical solution to this differential equation is of the form

$$n_e(t) = C_2 t^{C_1}.$$

(10)

For an assumed bulk velocity of 20 km/s and a plasma temperature of 2 eV derived from simulation results [*Fletcher et al.*, 2015], the electron density drops to effectively zero within approximately 100 ns, or when the plasma is about 2 mm in size.

Second, we use a matrix sheath approximation [*Lieberman and Lichtenberg*, 2005] to obtain an upper bound on when the plasma has rarified enough to be fully penetrated by the external electric field. The sheath thickness is given by

$$s = \lambda_D \sqrt{\frac{2V_s}{T_e}} = \sqrt{\frac{2V_s \epsilon_0 k_B}{n_e q_e^2}}.$$

(11)

Assuming an inverse-cubic dropoff in plasma density as its radius increases, the plasma radius becomes smaller than the sheath thickness when the plasma is approximately 1 m in size.

From these two bounds, we conclude that the electron depletion radius at which we can apply the plume angle approximation from Equation 11 is within the range of 1 mm to 1 m. Figure 28 shows the predicted ion plume angle for three impactor sizes and three impact surface bias levels, spanning a range of 0.1 mm to 10 m in electron depletion radius.
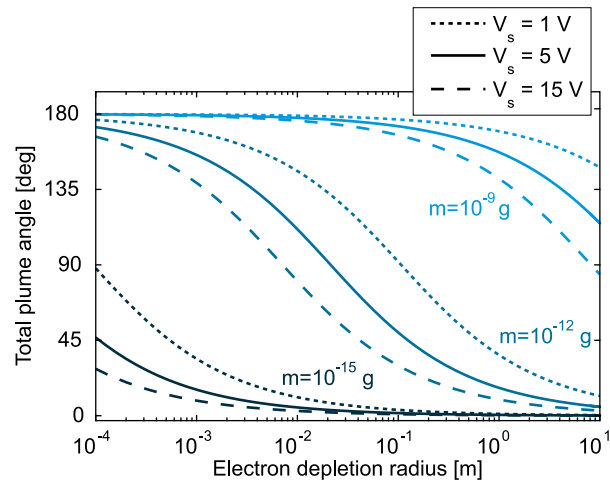
Figure 28: Total plume angle as a function of electron depletion radius.

The nanogram-sized impactors yield a near-hemispherical plume over the possible range of electron depletion radii over a range of surface bias from 1–15 V, while the smaller impactors result in a much smaller angle because of the reduced mutual electrostatic repulsion between the expanding ions. This is consistent with the narrower plume geometries detected in ground-based experiments using femtogram-sized impactors [*Goel*, 2016].

4.2   Meteoroid impact rate

Given the above analysis, we expect MIDEA's plasma sensors to be capable of detecting impacts of nanogram and larger meteoroids hitting the asteroid surface at speeds of 20 km/s and faster. In this section, we discuss the meteoroid impact rate and how this rate is affected by surface occlusions and orbital constraints.

4.2.1   Meteoroid flux models

The meteoroid population has been characterized using in situ impact detectors [*Mandeville and Berthoud*, 1995], Earth-based optical and radar meteor observations [*Close et al.*, 2008; *Musci et al.*, 2012], and crater analysis [*Werner et al.*, 2002]. The Grün interplanetary flux model is based on an analysis of meteoroid collisions to predict the flux at 1 AU over a mass range from 10^{-18} g to 10 g [*Grün et al.*, 1985]. It uses data from spacecraft impact measurements, zodiacal light measurements, and microcraters found on lunar rock samples, and is often the reference used to calibrate other models at 1 AU.

Two physics-based models are currently used to provide meteoroid flux predictions beyond 1 AU. The Meteoroid Engineering Model (MEM) provides directionality and velocity distributions of the meteoroid flux, using a balance of forces to identify steady-state meteoroid

orbital distributions [*McNamara et al.*, 2005]. Empirical measurements are used to constrain the model, which is valid within the inner solar system between 0.2 and 2.0 AU for meteoroids from 10^{-6} to 10 g in mass. The Interplanetary Micrometeoroid Environment Model (IMEM) evolves the meteoroid population from known parent sources, including asteroid and comet families, and constrains the source contributions using empirical measurements [*Dikarev et al.*, 2005]. This model is applicable between 0.1 and 10 AU for meteoroids between 10^{-18} and 1 g in mass [*Drolshagen et al.*, 2008].

Generally, smaller meteoroids are more numerous, and the MIDEA concept requires a trade-off between the signal strength produced by larger meteoroids and the higher impact rate of smaller meteoroids. For this study, MEM results were extrapolated from the microgram to nanogram range using the Grün model. Since the orbit of 2008 EV5 lies close to 1 AU, the Grün model remains valid down to the population of nanogram-sized meteoroids relevant to MIDEA, and the trends based on geometry and orbit are still applicable.

4.2.2 Meteoroid impact rate calculation

MEM provides meteoroid flux distributions corresponding to a seven-state vector composed of the Julian date and 3D position and velocity coordinates of the body of interest. The states associated with numerous solar system bodies can be obtained from JPL's HORIZONS system, or computed from their orbital elements. The output meteoroid flux is provided by MEM as speed- and direction-binned values, as well as integrated speed-binned values for surfaces facing particular directions (e.g., ram, sun-facing). The integrated sun-facing flux (summed over the speed bins exceeding 20 km/s) provides an overestimate on the impact rate of interest, because it does not account for the rotation of the asteroid surface into darkness, and the occlusion of surfaces due to the local horizon of the asteroid. We therefore use the full speed and direction distribution output of the MEM and a triangulated surface model of the asteroid shape to compute the meteoroid impact rate over the surface of the asteroid. To simplify the analysis, we use the short rotational period relative to the orbital period to obtain an impact rate averaged over the asteroid's rotation for a fixed orbital state.

For a particular meteoroid flux direction and asteroid surface facet, we express the flux radiant unit vector $\hat{n}_\mathrm{f}$ and surface normal unit vector $\hat{n}_\mathrm{s}$ in spherical coordinates using a reference frame aligned with the asteroid spin axis $\hat{k}$.

$$\hat{n}_\mathrm{f} = \begin{bmatrix} \cos\theta_\mathrm{f}\cos\phi_\mathrm{f} & \cos\theta_\mathrm{f}\sin\phi_\mathrm{f} & \sin\theta_\mathrm{f} \end{bmatrix}^\mathrm{T} \tag{12}$$

and

$$\hat{n}_\mathrm{s} = \begin{bmatrix} \cos\theta_\mathrm{s}\cos\phi_\mathrm{s} & \cos\theta_\mathrm{s}\sin\phi_\mathrm{s} & \sin\theta_\mathrm{s} \end{bmatrix}^\mathrm{T}, \tag{13}$$

where ϕ_f and ϕ_s are the right ascension relative to an arbitrary longitude, and θ_f and θ_s are the declination from the equatorial plane of the asteroid.

The contribution from this flux direction onto the rotating surface is weighted by η, relative to a fixed surface perpendicular to the flux direction, where

$$\eta = \frac{1}{2\pi} \int_{\phi_-}^{\phi_+} \hat{n}_f \cdot \hat{n}_s \, d\phi. \tag{14}$$

The integrand is

$$\hat{n}_f \cdot \hat{n}_s = \cos\theta_f \cos\theta_s \cos(\phi_f - \phi_s) + \sin\theta_f \sin\theta_s$$
$$= \cos\theta_f \cos\theta_s \cos(\Delta\phi) + \sin\theta_f \sin\theta_s, \tag{15}$$

eliminating the arbitrary reference longitude used to define the right ascension angle.

The limits of integration are based on the surface orientation, the local horizon, and the sun direction and orbital constraints. For the flux to make a non-zero contribution, the surface normal must project in a positive sense on the radiant vector, or

$$\cos\theta_f \cos\theta_s \cos(\Delta\phi) + \sin\theta_f \sin\theta_s > 0, \tag{16}$$

which yields

$$|\Delta\phi| < \phi_t = \begin{cases} \pi, & \text{for } \tan\theta_s \tan\theta_f > 1; \\ 0, & \text{for } \tan\theta_s \tan\theta_f < -1; \\ \cos^{-1}(-\tan\theta_s \tan\theta_f), & \text{otherwise.} \end{cases} \tag{17}$$

The local horizon is approximated by expressing the vertices of the asteroid model in spherical coordinates in a frame centered on the surface in question, where the zenith direction $\hat{z}$ is aligned with the asteroid spin axis $\hat{k}$ and the surface normal $\hat{n}_s$ is in the xz-plane. The local horizon ϕ_{h+} and ϕ_{h-} in terms of $\Delta\phi$ can then be found as a function of declination.

Figure 29 shows the asteroid vertices plotted in the local cylindrical frame associated with one facet of the shape model. This particular facet is located in the northern hemisphere and is therefore occluded from any meteoroid flux below approximately -45 degrees elevation. The horizon limits are plotted in blue and red; the dashed lines indicate the limits based on the orientation of the facet itself, and the solid lines account for the occlusion from vertices of the asteroid that extend beyond the plane of the facet. Note that the additional occlusion from the geometry of the asteroid above the plane of a facet would only affect meteoroid flux directions that are already presented with a very small projected area, so the overall surface impact rate is not substantially reduced by this effect.
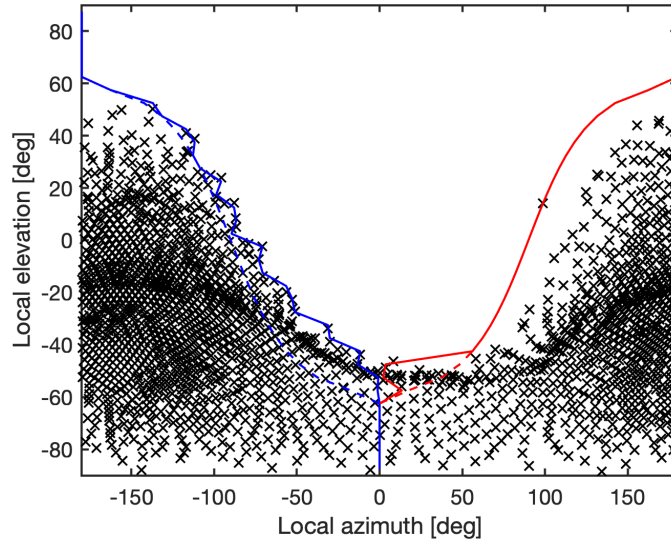
Figure 29: Local azimuth visibility bounds seen from the centroid of one facet of the asteroid shape model, showing the flat plate horizon (dashed lines) and actual local horizon horizon (solid line), as well as the asteroid vertices in the local cylindrical frame.

Finally, the sun angle and orbital visibility constraint is found from the orbital state vector of the asteroid. In a frame aligned with the asteroid velocity and the orbit normal, the sun angle is

$$\psi_\odot = \pi - \cos^{-1}(\hat{v} \cdot \hat{r}), \tag{18}$$

where $\hat{v}$ and $\hat{r}$ are unit vectors in the asteroid velocity and anti-helion directions. The range of surface orientations which are exposed to the sun is therefore

$$\psi_\odot - \pi/2 - \phi_f < \Delta\phi < \psi_\odot + \pi/2 - \phi_f \tag{19}$$

relative to the incoming meteoroid flux. In prior work, we considered any impacts on the sunlit hemisphere to be detectible by the orbiting MIDEA constellation. However, based on the polar orbit identified in this work, the plasma sensors may not be able to see impacts that occur too far from the terminator region. To approximate this effect, we extended our encoded integration boundaries to only consider meteoroids approaching from a prescribed angular sector relative to the asteroid velocity direction.

Figure 30 shows the integration limits imposed on the incoming meteoroid flux for a ±45 degree sector offset from the velocity direction by 45 degrees, i.e. for just the first quadrant. Here the red and blue lines indicate the azimuth range *relative to the azimuth of the meteoroid source*. In this case, a meteoroid source coming from an azimuth of 0 degrees should be able to impact a surface oriented anywhere from -90 degrees to +90 degrees, but only the 0 to 90 degree range is considered. A meteoroid source at 180 degrees (the anti-ram direction) will just barely catch facets at +90 degrees (lagging -90 degrees behind the source) as it rotates into view and immediately out of the sector of interest. These azimuth ranges modify the inequality used in equation 19, which only captures the sunlit hemisphere.
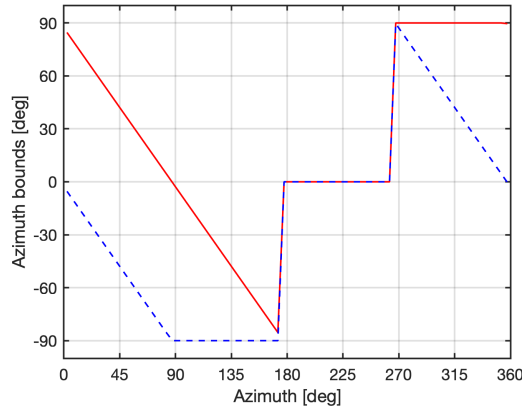
Figure 30: Azimuth visibility bounds applied for a ±45 degree sector centered at 45 degrees.

Combining these three constraints, the limits of integration can be expressed as

$$\phi_+ = \min(\phi_{\text{t}}, \phi_{\text{h}+}, \psi_\odot + \pi/2 - \phi_{\text{f}}),$$
$$\phi_- = \max(-\phi_{\text{t}}, \phi_{\text{h}-}, \psi_\odot - \pi/2 - \phi_{\text{f}}). \tag{20}$$

Equation 14 can then be integrated in closed form, giving

$$\eta = \cos\theta_{\text{f}}\cos\theta_{\text{s}}\,(\sin\phi_+ - \sin\phi_-) + \sin\theta_{\text{f}}\sin\theta_{\text{s}}\,(\phi_+ - \phi_-). \tag{21}$$

The total flux on a particular surface, averaged over the asteroid rotation, is then the sum over all of the incoming flux directions, weighted by η. Figure 31 illustrates the effect of this weighting. On the left, the unadjusted directional flux from MEM is plotted over the directional sphere, showing two major sources at azimuths of approximately 90 and 270 degrees. On the right, the weighting is applied, eliminating the contribution of the source that will only result in impacts on the dark side of the asteroid.
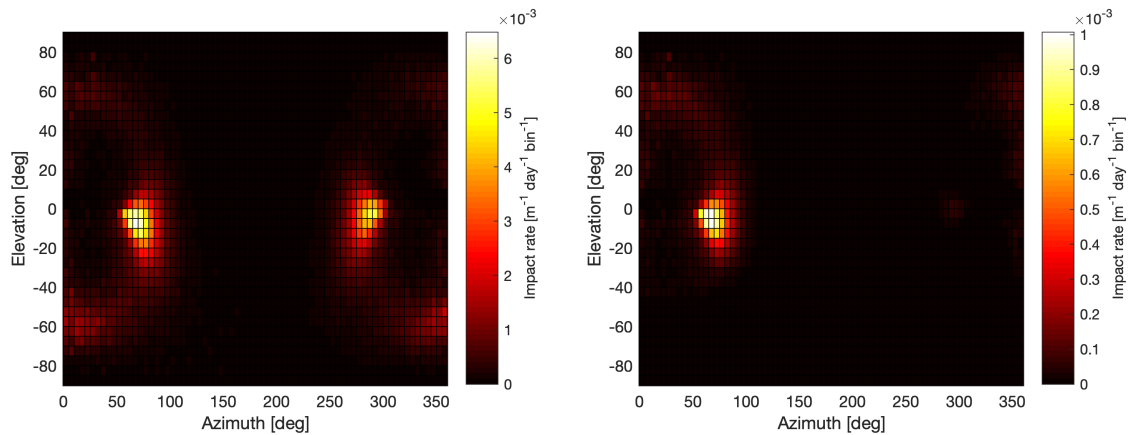
Figure 31: MEM spatial flux of nanogram-sized meteoroids in 5 degree bins traveling faster than 20 km/s (left) and the effective flux for one particular facet accounting for visibility limits (right).

4.2.3   Impact rate on 2008 EV5 and other bodies

A study of the impact rate of nanogram-sized meteoroids impacting the surface of a range of small solar system bodies was undertaken during the ESI project, and predicted an impact rate of approximately 0.05–0.12 m^{-2} day^{-1} for impacts exceeding 20 km/s, as shown in Figure 29 [*Lee and Close*, 2016].
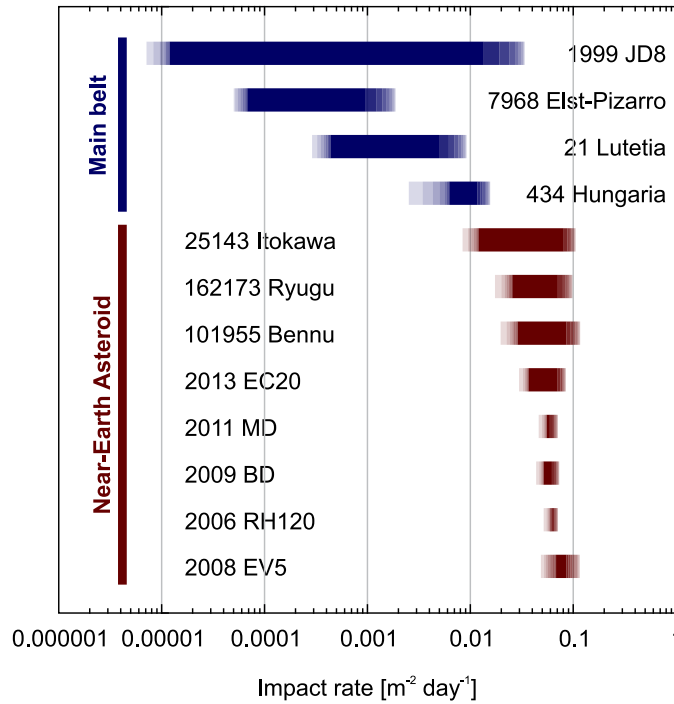
Figure 32: Range of nanogram impact rates >20 km/s for selected small solar system bodies.

Figure 33 shows the spatial distribution of impact rates over the surface of 2008 EV5 at four points along its orbit, while Figure 34 shows the result of this analysis over its full orbit. The impact rates show that the impact rate over 90% of the surface remains between 0.05 and 0.12 m^{-2} day^{-1} for impacts exceeding 20 km/s, along the entire orbit. However, this flux distribution does not account for the constraint of flying the plasma sensors in a single polar orbital plane, which limits the coverage of the sensor constellation.
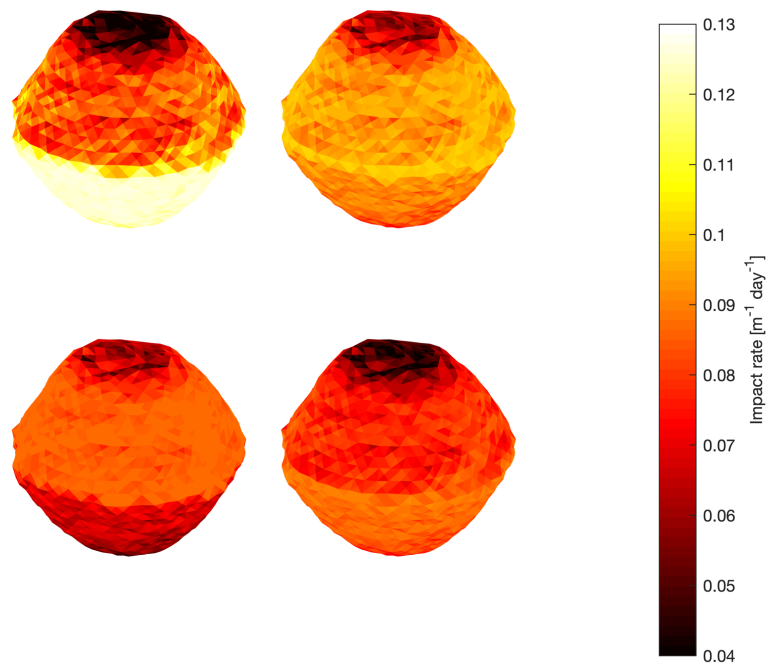
Figure 33: Spatial map of impact rate over the surface of 2008 EV5 from nanogram-sized meteoroids at four points along its orbit.
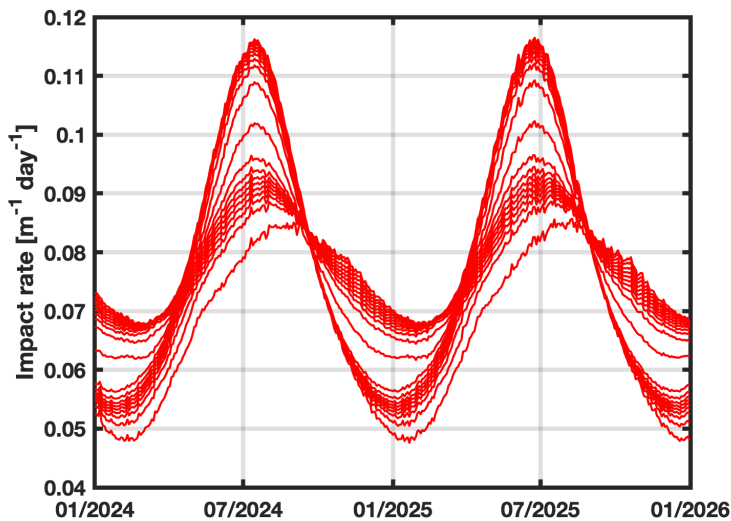
Figure 34: Impact rate over the orbit of 2008 EV5, shown at 5 percentile intervals over the surface area of a model sphere.

Using the directional meteoroid flux output by MEM, we show in Figure 35 how the effective impact rate drops as the angle of visibility decreases from 180 degrees (the full sunlit hemisphere) down to a 10 degree sector in the ram direction. With the nominal orbit radius of 400 m around an asteroid with a diameter of approximately 400 m, the angle of visibility should be approximately 60 degrees. This assumes a near hemispherical plasma plume where ejecta from

an impact on the horizon will still reach the plasma sensors. In this case, the area-normalized median impact rate is 0.076 m^{-2} day^{-1}, with 95% of the surface experiencing an impact rate of 0.0457 m^{-2} day^{-1} or greater, while some areas will see up to 0.0944 impacts m^{-2} day^{-1}.
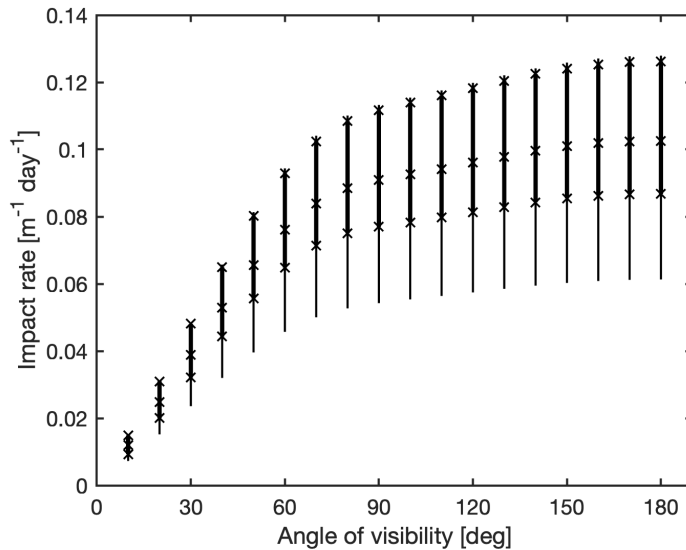
Figure 35: Range of impact rates as a function of angle of visibility, measured from the asteroid velocity direction and increasing toward the sun direction. The thin lines span the 5th to 95th percentiles by surface area, while the thick lines indicate the interquartile range and the x markers specify the quartiles and median.

4.3 Mission duration

Using the value of 0.0457 m^{-2} day^{-1} as a minimum impact rate, meteoroid impacts will fully "sample" the asteroid surface at 1 m resolution within a period of 22 days. While some system inefficiencies are expected to increase this required mission duration, such as missed detections and time to deploy and commission the sensor spacecraft, the angle of visibility analysis is also conservative in terms of the impacts that can be seen closer to the polar regions. Based on these factors, the results from our study are consistent with completing a full MIDEA mission within 30–50 days. In contrast, the small area of sensitive electronics on the sensors will sustain a damaging impact at a rate no greater than once every five months.

Given the planar orbital geometry at 400 m radius, three precisely positioned sensors uniformly spaced apart would provide 360 degree coverage of the terminator region. However, this would allow for very little redundancy if any individual sensor is lost, and necessitate more stringent requirements on the control of the MIDEA constellation geometry even when all sensors are operational. Instead, we envision a constellation of four to six sensors to be a reasonable number to provide constant coverage of the asteroid surface. As sensors fail, the constellation can be adjusted to compensate for the loss of coverage by sacrificing regions of redundant observability. A benefit of the MIDEA architecture is that if a mission is terminated prematurely, the partial data returned would still produce a global map of the asteroid, albeit at a lower spatial resolution or with lower confidence on the elemental composition.

5   Conclusions

The objective of this NIAC Phase I study was to demonstrate feasibility of the MIDEA architecture in the context of proximity operations around an asteroid target and to develop the design of an orbital geometry and attitude control strategy for the ultralight plasma sensors. In this section, we review the major findings of the study and discuss avenues of future work to build on these results.

5.1   Summary of findings

A 2024–2026 mission to 2008 EV5 can be accomplished with post-insertion delta V of 0.45 km/s.

Our survey of heliocentric rendezvous trajectories to 2008 EV5 showed multiple opportunities over the next few decades to reach the asteroid with propulsive requirements that are achievable through technologies that will be available in the near future. The candidate trajectory reaching the asteroid in mid-2026 requires only 0.45 km/s delta V at the asteroid, which is within the capability of a 12U hybrid propulsion system being designed.

The ultralight plasma sensors must be deployed into a polar terminator orbit to maintain stability over the duration of the mission.

The dynamics of orbits under substantial solar radiation pressure require the disturbance force to be primarily directed in the orbit normal to avoid ejection from the parent body. This restricts the plasma sensor constellation to polar orbits that are aligned with the terminator.

The design mass of the plasma sensors must be increased to 250 g for robustness against uncertainties in the total asteroid mass.

To ensure the stability of the polar orbit given the uncertainty in total asteroid mass, the design mass of the sensor spacecraft was increased to 250 g from the initial target of 100 g. This relaxes the aggressive lightweight design of the sensor spacecraft and allows for more conventional mechanical designs to be used for the solar panels, including rigid PCBs rather than relying on membrane structures with lower flight heritage.

Controlled reflectivity provides sufficient actuation authority to maintain attitude control of the plasma sensors.

Our proposed geometry for the plasma sensors including a perpendicular plasma sensor electrode, two deployable plasma sensors, and canted reflector vanes, provides a favorable mass distribution for dynamic stability of the spacecraft attitude relative to the sun direction. A discrete switching line control law for actuating controlled reflectivity devices on the reflector vanes demonstrated rapid regulation for sun pointing from a wide range of initial offset angles.

The total required mission duration is not substantially increased by consideration of orbital constraints.

The reduction of detectable meteoroid impacts on the asteroid surface due to the visibility from a polar terminator orbit results in a slight reduction from the impact rate over the full sunlit hemisphere, as long as the plasma plume expansion is wide. A narrower expansion plume would further limit the observable impacts from closer to the horizon. A 30–50 day mission duration is expected to provide 1 m resolution in forming a composition map of the asteroid surface.

5.2   Next steps

Several aspects of the MIDEA architecture require further analysis to achieve the ultimate goal of bringing the cost of asteroid exploration down to a level where commercial entities or other non-governmental organizations could afford to undertake such a mission. In particular, a major priority for further study is to address the launch configuration and the strategy to send multiple MIDEA missions in parallel to multiple asteroid targets. This study would involve identifying asteroids that would be reachable through a similar rendezvous orbit, which would facilitate using a single large Earth departure stage rather than staging individual departures from a secondary launch orbit, such as a translunar transfer orbit.

The MIDEA architecture also requires further development of the sensor localization and constellation formation maintenance strategy using a combination of radiofrequency ranging and optical navigation. We expect that this aspect of the MIDEA concept will benefit from developments in the Autonomous Nanosatellite Swarming (ANS) project, which proposes to design a Dynamics, Guidance, Navigation, and Control (DGN&C) set of algorithms that can be distributed and deployed on a swarm of cooperative nanosatellites to achieve autonomous fuel-optimal operations for a broad class of asteroids while simultaneously characterizing the asteroids' shape, gravity, and dynamical properties [*Stacey and D'Amico*, 2018]. Despite the differences between the reference architectures in the ANS project and MIDEA, there are many aspects of the proposed ANS algorithms that are relevant and can be adapted to jumpstart an equivalent navigation subsystem for MIDEA. In particular, the concept that multiple satellites (or agents) can behave as a single spacecraft through precise relative navigation (between agents) and by exchanging remote sensing data through inter-satellite links can apply to the MIDEA constellation, and the optical sensor fusion techniques for pose estimation of the asteroid as well as the radiofrequency ranging techniques for triangulating the individual agents' position and orientation are both directly relevant to the MIDEA architecture.

Finally, a concurrent engineering design effort is necessary to capture the many subsystems needed to implement the MIDEA architecture from the Earth departure stage and mothership to the multiple free-flying plasma sensor spacecraft. A complete convergent design would provide a starting point for establishing mission cost estimates and identifying a required technology development roadmap to validate and demonstrate the MIDEA architecture and eventually undertaking asteroid exploration missions.

6   References

Arya, M., Lee, N., and Pellegrino, S., "Ultralight Structures for Space Solar Power Satellites," *3rd AIAA Spacecraft Structures Conference*, No. AIAA 2016-1950, San Diego, California, USA, 2016, doi: 10.2514/6.2016-1950.

Atchison, J. A. and Peck, M. A., "A passive, sun-pointing, millimeter-scale solar sail," *Acta Astronautica*, Vol. 67, No. 1, 2010, pp. 108–121, doi: 10.1016/j.actaastro.2009.12.008.

Atchison, J. A., Mitch, R., Apland, C., Kee, C., Rivkin, A., Mazarico, E., Harclerode, K., Wortman, J., and Candela, K., "NIAC Swarm Flyby Gravimetry," *NIAC Phase II final report*, 2017.

Atchison, J., Mitch, R., and Rivkin, A., "Swarm Flyby Gravimetry," *NIAC Phase I final report*, 2015.

Auer, S., Grün, E., Rauser, P., Rudolph, V., and Sitte, K., "Studies on simulated micrometeoroid impact," *Space Research VIII*, 1968, pp. 606–616.

Beech, M., and Steel, D., "On the Definition of the Term 'Meteoroid'," *Quarterly Journal of the Royal Astronomical Society*, Vol. 36, No. 3, 1995, pp. 281–284.

Beshore, E., et al., "The OSIRIS-Rex asteroid sample return mission," *IEEE Aerospace Conference*, 2015, doi:10.1109/AERO.2015.7118989.

Block, L. P., "A Double Layer Review," *Astrophysics and Space Science*, Vol. 55, No. 1, 1978, pp. 59–83, doi:10.1007/BF00642580

Bottke, W. F., Durda, D. D., Nesvorny, D., Jedicke, R., Morbidelli, A., Vokrouhlicky, D., and Levison, H., "The Fossilized Size Distribution of the Main Asteroid Belt," *Icarus*, Vol. 175, No. 1, 2005, pp. 111–140, doi:10.1016/j.icarus.2004.10.026.

Burchell, M., Cole, M. J., and Ratcliff, P. R., "Light flash and ionization from hypervelocity impacts on ice," *Icarus*, Vol. 122, No. 2, 1996, pp. 359–365, doi: 10.1006/icar.1996.0129.

Bus, S. J., and Binzel, R. P., "Phase II of the Small Main-Belt Asteroid Spectroscopic Survey: A Feature-Based Taxonomy," *Icarus*, Vol. 158, No. 1, 2002, pp. 146–177, doi:10.1006/icar.2002.6856.

Busch, M. W., et al., "Radar observations and the shape of near-Earth ASTEROID 2008 EV5," *Icarus*, Vol. 212, 2011, pp. 649–660, doi: 10.1016/j.icarus.2011.01.013.

Bush, K. A., et al., "23.6%-Efficient Monolithic Perovskite/Silicon Tandem Solar Cells with Improved Stability," *Nature Energy*, Vol. 2, No. 4, 2017, Paper 17009. doi:10.1038/nenergy.2017.9.

Castillo-Rogez, J., CubeSat for Planetary Science and Exploration, *Achieving Science Goals with CubeSats Community Symposium*, Irvine, CA, 2015.

Chapman, C. R., Morrison, D., and Zellner, B., "Surface Properties of Asteroids: A Synthesis of Polarimetry, Radiometry, and Spectrophotometry," *Icarus*, Vol. 25, No. 1, 1975, pp. 104–130, doi:10.1016/0019-1035(75)90191-8.

Chujo, T., Ishida, H., Mori, O., and Kawaguchi, J., "Liquid crystal device with microstructure for attitude control of spacecraft by solar radiation pressure," *AIAA Space Flight Mechanics Meeting, AIAA SciTech Forum*, Paper AIAA 2018-0964, doi: 10.2514/6.2018-0964.

Close, S., Hamlin, T., Oppenheim, M., Cox, L., and Colestock, P., "Dependence of Radar Signal Strength on Frequency and Aspect Angle of Nonspecular Meteor Trails," *Journal of Geophysical Research*, Vol. 113, No. A6, June 2008, Paper A06203. doi:10.1029/2007JA012647.

Close, S., Linscott, I., Lee, N., Johnson, T., Strauss, D., Goel, A., Lauben, D., Srama, R., Mocker, A., and Bugiel, S., "Detection of electromagnetic pulses produced by hypervelocity micro particle impact plasmas," *Phys Plasmas*, Vol. 20, No. 092102, 2013, pp. 1–8, doi:10.1063/1.4819777.

Cohen, M. M., James, W. W., Zacny, K., Craft, J., Chu, P., and Blair, B., "Robotic Asteroid Prospector (RAP)," *NIAC Phase I final report*, 2013.

Crawford, D. and Schultz, P., "Electromagnetic properties of impact-generated plasma, vapor and debris," *International Journal of Impact Engineering*, Vol. 23, No. 1, 1999, pp. 169–180.

De Sanctis, M. C., et al., The VIR spectrometer, *Space Sci Rev*, Vol. 163, 2011, pp. 329–369, doi:10.1007/s11214-010-9668-5.

Dietzel, H., Eichhorn, G., Fechtig, H., Grün, E., Hoffmann, H.-J., Kissel, J., "The HEOS 2 and HELIOS micrometeoroid experiments," *Journal of Physics E: Scientific Instruments*, Vol. 6, No. 3, 1973, 209–217, doi:10.1088/0022-3735/6/3/008.

Dietzel, H., Neukum, G., and Rauser, P., "Micrometeoroid simulation studies on metal targets," *Journal of Geophysical Research*, Vol. 77, No. 8, 1972, pp. 1375–1395, doi: 10.1029/JB077i008p01375.

Dikarev, V., Grün, E., Baggaley, J., Galligan, D., Landgraf, M., and Jehn, R., "The New ESA Meteoroid Model," *Advances in Space Research*, Vol. 35, No. 7, 2005, pp. 1282–1289. doi:10.1016/j.asr.2005.05.014.

Draine, B. T., "Interstellar dust grains," *Annual Review of Astronomy and Astrophysics*, Vol. 41, 2003, pp. 241–289, doi: 10.1146/annurev.astro.41.011802.094840.

Drapatz, S., and Michel, K. W., "Theory of shock-wave ionization upon high-velocity impact of micrometeorites," *Zeitschrift Naturforschung Teil A*, Vol. 29, 1974, pp. 870–879.

Drolshagen, G., "Comparison of Meteoroid Models," Tech. Rep. IADC-09-03, *Inter-Agency Space Debris Coordination Committee*, 2009.

Drolshagen, G., Dikarev, V., Landgraf, M., Krag, H., Kuiper, W., "Comparison of meteoroid flux models for near Earth space," *Earth, Moon, and Planets*, Vol. 102, No. 1–4, 2008, pp. 191–197, doi:10.1007/s11038-007-9199-6.

Eperon, G. E., et al., "Perovskite-Perovskite Tandem Photovoltaics with Optimized Band Gaps," *Science*, Vol. 354, No. 6314, 2016, pp. 861–865. doi:10.1126/science.aaf9717.

Fletcher, A. and Close, S., "Simulating hypervelocity impact plasmas and their effects on spacecraft," *URSI-USNC National Radio Science Meeting*, Boulder, CO, 2014.

Fletcher, A., Close, S., Mathias, D., "Simulating plasma production from hypervelocity impacts," *Physics of Plasmas*, Vol. 22, No. 093504, 2015, doi:10.1063/1.4930281.

Friichtenicht, J. F., "Two-million-volt electrostatic accelerator for hypervelocity research," *Rev Sci Instrum*, Vol. 33, No. 2, 1962, pp. 209–212, doi:10.1063/1.1746548.

Frost, V. C., Meteoroid damage assessment, *Tech. Rep. SP-8042*, NASA, 1970.

Gellert, R., et al., "In situ compositional measurements of rocks and soils with the alpha particle x-ray spectrometer on NASA's Mars rovers," *Elements*, Vol. 11, 2015, pp. 39–44, doi: 10.2113/gselements.11.1.39.

Goel, A., "Detection and Characterization of Meteoroid and Orbital Debris Impacts in Space," Ph.D. Thesis, Stanford Univ., Stanford, CA, 2016.

Goel, A., Tarantino, P. M., Lauben, D. S., and Close, S., "Design and testing of miniaturized plasma sensor for measuring hypervelocity impact plasmas," *Review of Scientific Instruments*, Vol. 86, No. 4, Paper 043304, 2015, pp. 1–14, doi: 10.1063/1.4917276.

Grün, E., Zook, H. A., Fechtig, H., and Giese, R. H., "Collisional balance of the meteoritic complex," *Icarus*, Vol. 62, No. 2, 1985, pp. 244–272, doi: 10.1016/0019-1035(85)90121-6.

Hemmati, H., Willis, P., Roberts, T., Castillo, J., Sengupta, A. and McElrath, T., "Two-dimensional planetary surface landers," *NIAC Phase 1 final report*, 2014.

Hodges, R. E., Hoppe, D. J., Radway, M. J., and Chahat, N. E., "Novel Deployable Reflectarray Antennas for CubeSat Communications," *2015 IEEE MTT-S International Microwave Symposium*, 2015, doi: 10.1109/MWSYM.2015.7167153.

Hoyt, R., James, K., Slostad, J., and Moser, T., "WRANGLER: Capture and de-spin of asteroids & space debris," *NIAC Phase I final report*, 2015.

Jansen, R., Teegarden, E., and Gimelshein, S., "Characterization of a Vortex-flow End-burning Hybrid Rocket Motor for Nanosatellite Applications" *50th AIAA Aerospace Sciences Meeting*, AIAA 2012-0125, 2012, doi: 10.2514/6.2012-125.

Janson, S. W., "Brane Craft," *NIAC Phase I final report*, 2017.

Jens, E. T., Mechentel, F. S., Cantwell, B., J., and Hubbard, G. S., "Combustion visualization of paraffin-based hybrid rocket fuel at elevated pressures," *50th AIAA/ASME/SAE/ASEE Joint Propulsion Conference*, AIAA 2014-3848, 2014, doi: 10.2514/6.2014-3848.

Jens, E., Karp, A. C., Rabinovitch, J., Nakazono, B., Conte, A., and Vaughan, D., "Design of interplanetary hybrid CubeSat and SmallSat propulsion systems," *2018 Joint Propulsion Conference, AIAA Propulsion and Energy Forum,* Paper AIAA 2018-4668, doi: 10.2514/6.2018-4668.

Kivelson, M. G., and Russell, C. T. (eds.), *Introduction to Space Physics*, Cambridge Univ. Press, New York, 1995, p. 92.

Kolosa, D., Spangelo, S., Lemmer, K., and Hudson, J., "Mission Analysis for a Micro RF Ion Thruster for CubeSat Orbital Maneuvers," *50th AIAA/ASME/SAE/ASEE Joint Propulsion Conference*, AIAA 2014-3908, 2014, doi: 10.2514/6.2014-3908.

Lee, N. and Close, S., "Meteoroid Impact Detection for Exploration of Asteroids (MIDEA): A concept for asteroid prospecting," *Meteoroids 2016*, 2016.

Lee, N. and Close, S., "Meteoroid Impact Detection for Exploration of Asteroids: Small satellites for asteroid characterization," *Journal of Spacecraft and Rockets*, 2017, doi: 10.2514/1.A33928.

Lee, N., Close, S., Goel, A., Lauben, D., Linscott, I., Johnson, T., Strauss, D., Bugiel, S., Mocker, A., and Srama, R., "Theory and experiments characterizing hypervelocity impact plasmas on biased spacecraft materials," *Physics of Plasmas*, Vol. 20, 032901, 2013, doi: 10.1063/1.4794331.

Lee, N., Close, S., Lauben, D., Linscott, I., Goel, A., Johnson, T., Yee, J., Fletcher, A., Srama, R., Bugiel, S., Mocker, A., Colestock, P., and Green, S., "Measurements of freely-expanding plasma from hypervelocity impacts," *Int J Impact Eng*, Vol. 44, 2012, pp. 40–49, doi:10.1016/j.ijimpeng.2012.01.002.

Lee, N., Goel, A., and Close, S., "Hypervelocity impact plasma expansion: scaling from experiment to space," *URSI-USNC National Radio Science Meeting*, 2017.

Lewis, J. S., "In-space production of storable propellants," *NIAC Phase I final report*, 2016.

Li, A. and Draine, B. T., "Infrared emission from interstellar dust. II. The diffuse interstellar medium," *Astrophysical Journal*, Vol. 554, 2001, pp. 778–802, doi: 10.1086/323147.

Lieberman, M. A., and Lichtenberg, A. J., "Direct Current (DC) Sheaths," *Principles of Plasma Discharges and Materials Processing*, 2nd ed., Wiley, Hoboken, NJ, 2005, pp. 165–206, Chap. 6. doi:10.1002/0471724254.ch6.

Llanos, P. J., Miller, J. K., and Hintz, G. R., "Orbital evolution and environmental analysis around asteroid 2008 EV5," *24th AAS/AIAA Space Flight Mechanics Meeting*, Paper AAS 14-360.

Mach, P., Rodriguez, S. J., Nortrup, R., Wiltzius, P., and Rogers, J. A., "Monolithically integrated, flexible display of polymer-dispersed liquid crystal driven by rubber-stamped organic thin-film transistors," *Applied Physics Letters*, Vol. 78, No. 23, 2001, pp. 3592–3594, doi: 10.1063/1.1377312.

Mainzer, A., et al., "NEOWISE Observations of Near-Earth Objects: Preliminary Results," *Astrophysical Journal*, Vol. 743, No. 2, 2011, p. 156, doi:10.1088/0004-637X/743/2/156.

Manchester, Z., Peck, M., and Filo, A., "KickSat: A crowd-funded mission to demonstrate the world's smallest spacecraft," *AIAA/USU Conference on Small Satellites*, Paper SSC13-IX-5, 2013.

Mandeville, J. C., and Berthoud, L., "From LDEF to EURECA: Orbital Debris and Meteoroids in Low Earth Orbit," *Advances in Space Research*, Vol. 16, No. 11, 1995, pp. 67–72. doi:10.1016/0273-1177(95)98754-C.

Martel, F., Perna, L., and Lozano, P., "Miniature ion electrospray thrusters and performance tests on CubeSats," *26th Annual AIAA/USU Conference on Small Satellites*, SCC12-VI-5, 2012.

Mazanek, D. D., Merrill, R. G., Brophy, J. R., and Mueller, R. P., "Asteroid Redirect Mission concept: A bold approach for utilizing space resources," *65th International Astronautical Congress*, Toronto, Canada, 2014.

McBride, N., and McDonnell, J. A. M., "Meteoroid Impacts on Spacecraft: Sporadics, Streams, and the 1999 Leonids," *Planetary and Space Science*, Vol. 47, Nos. 8–9, 1999, pp. 1005–1013, doi:10.1016/S0032-0633(99)00023-9.

McKnight, B. R., Armold, D., Boyer, J. E., Kuo, K. K., DeSain, J. D., Fuller, J. K., Brady, B. B., and Curtiss, T. J., "Testing of Hybrid Rocket Fuel Grains at Elevated Temperatures with Swirl Patterns Fabricated Using Rapid Prototyping Technology," *50th AIAA/ASME/SAE/ASEE Joint Propulsion Conference & Exhibit*, AIAA Paper 2014-3754, 2014, pp. 1–13. doi:10.2514/6.2014-3754.

McNamara, H., Jones, J., Kauffman, B., Suggs, R., Cooke, W., and Smith, S., "Meteoroid Engineering Model (MEM): A Meteoroid Model for the Inner Solar System," *Earth, Moon and Planets*, Vol. 95, Nos. 1–4, 2005, pp. 123–139. doi:10.1007/s11038-005-9044-8.

Meech, K. J., R. Weryk, M. Micheli, J. T. Kleyna, O. R. Hainaut, R. Jedicke, R. J. Wainscoat, K. C. Chambers, J. V. Keane, A. Petric, L. Denneau, E. Magnier, T. Berger, M. E. Huber, H. Flewelling, C. Waters, E. Schunova-Lilly and S. Chastel, "A brief visit from a red and

extremely elongated interstellar asteroid," *Nature*, Vol. 552, 2017, pp. 378–381, doi:10.1038/nature25020.

Melosh, H. J., 1989. Impact cratering: A geologic process. Oxford University Press (Oxford Monographs on Geology and Geophysics, No. 11), New York.

Morrow, E., D. J. Scheeres, and D. Lubin, "Solar sail orbit operations at asteroids," *Journal of Spacecraft and Rockets*, Vol. 38, No. 2, 2001, pp. 279–286, doi: 10.2514/2.3682.

Musci, R., Weryk, R. J., Brown, P., Campbell-Brown, M. D., and Wiegert, P. A., "An Optical Survey for Millimeter-Sized Interstellar Meteoroids," *Astrophysical Journal*, Vol. 745, No. 2, Article 161, 2012, pp. 1–6. doi:10.1088/0004-637X/745/2/161.

National Research Council, Limiting future collision risk to spacecraft: An assessment of NASA's meteoroid and orbital debris programs, *Report of the Committee for the Assessment of NASA's Orbital Debris Programs, D. Kessler, Chair, National Academy of Sciences*, 2011a.

National Research Council, Vision and Voyages for Planetary Science in the Decade 2013–2022, *Report of the Committee on the Planetary Science Decadal Survey, S. Squyres, Chair, National Academy of Sciences*, 2011b.

O'Brien, D. P., and Greenberg, R., "The Collisional and Dynamical Evolution of the Main-Belt and NEA Size Distributions," Icarus, Vol. 178, No. 1, 2005, pp. 179–212, doi:10.1016/j.icarus.2005.04.001.

Ono, M., Quadrelli, M., Lantoine, G., Backes, P., Lopez Ortega, A., Grip, H., Yen, C.-W., and Jewitt, D., "Comet Hitchhiker," *NIAC Phase I final report*, 2015.

Pieters, C. M., et al., "Surface composition of Vesta: Issues and integrated approach," *Space Sci Rev*, Vol. 163, 2011, 117–139, doi:10.1007/s11214-011-9809-5.

Plescia, J., "Seismic exploration of small bodies," *NIAC Phase I final report*, 2016.

Prettyman, T. H., et al., Dawn's Gamma Ray and Neutron Detector, *Space Sci Rev*, Vol. 163, 2011, pp. 371–459, doi:10.1007/s11214-011-9862-0.

Prettyman, T. H., Koontz, S. L., Pinsky, L. S., Empl, A., Mittlefehldt, D. W., Reddell, B. D., and Sykes, M. V., "Deep mapping of small solar system bodies with galactic cosmic ray secondary particle showers," *NIAC Phase I final report*, 2014.

Ratcliff, P. R., Burchell, M. J., Cole, M. J., Murphy, T. W., Allahdadi, F., "Experimental measurements of hypervelocity impact plasma yield and energetics," *International Journal of Impact Engineering*, Vol. 20, No. 6-10, 1997, pp. 663–674, doi:10.1016/S0734-743X(97)87453-2.

Rovey, J. L., Yang, X., Friz, P. D., Hu, C., and Glascock, M. S., "Plasmonic force propulsion revolutionizes nano/picosatellite capability," *NIAC 2013 Phase I final report*, 2014.

Russell, C. T. and Raymond, C. A., "The Dawn mission to Vesta and Ceres," *Space Sci Rev*, Vol. 163, 2011, pp. 3–23, doi:10.1007/s11214-011-9836-2.

Saiki, T., et al., "Attitude operation results of solar sail demonstrator IKAROS," *28th International Symposium on Space Technology and Science*, 2012, doi: 10.2322/tastj.10.To_4_1.

Santo, A. G., Lee, S. C., and Gold, R. E., "NEAR spacecraft and instrumentation," *J. Astronaut Sci*, Vol. 43, No. 4, 1995, pp. 373–397.

Scheeres, D. J., "Satellite dynamics about small bodies: Averaged solar radiation pressure effects," *J. Astronautical Sciences*, Vol. 47, No. 1, 1999, pp. 25–46.

Schlegel, D. J., Finkbeiner, D. P., and Davis, M., "Maps of dust infrared emission for use in estimation of reddening and cosmic microwave background radiation foregrounds," *The Astrophysical Journal*, Vol. 500, 1998, pp. 525–553, doi: 10.1086/305772.

Sercel, J., "Asteroid Provided In-situ Supplies (APIS): A breakthrough to enable an affordable NASA program of human exploration and commercial space industrialization," *NIAC Phase I final report*, 2016.

Sheehan, J. P., Collard, T. A., Longmier, B. W., and Goglio, I. M., "New Low-Power Plasma Thruster for Nanosatellites," *50th AIAA/ASME/SAE/ASEE Joint Propulsion Conference*, AIAA 2014-3914, 2014, doi: 10.2514/6.2014-3914.

Sheraw, C. D., Zhou, L., Huang, J. R., Gundlach, D. J., Jackson, T. N., Kane, M. G., Hill, I. G., Hammond, M. S., Campi, J., Greenling, B. K., Francl., J., and West, J., "Organic thin-film transistor-driven polymer-dispersed liquid crystal displays on flexible polymeric substrates," *Applied Physics Letters*, Vol. 80, No. 6, 2002, pp. 1088–1090, doi: 10.1063/1.1448659.

Sierks, H., et al., "The Dawn Framing Camera," *Space Sci Rev*, Vol. 163, 2011, pp. 263–327, doi:10.1007/s11214-011-9745-4.

Simmons, J. F. L. and McInnes, C. R., "Was Marx right? or How efficient are laser driven interstellar spacecraft?" *American Journal of Physics*, Vol. 61, No. 205, 1993.

Song, W., Li, J., and Ning, J., "Characteristics of plasma generated by hypervelocity impact," *Physics of Plasmas*, Vol. 20, 093501, 2013, doi:10.1063/1.4819829.

Squyres, S. W., et al., "Overview of the Opportunity Mars Exploration Rover mission to Meridiani Planum: Eagle Crater to Purgatory Ripple," *Journal of Geophysical Research*, Vol. 111, No. E12S12, 2006, doi: 10.1029/2006JE002771.

Srama, R., et al., "The Cassini Cosmic Dust Analyzer," *Space Science Reviews*, Vol. 114, No. 1, 2004, pp. 465–518, doi:10.1007/s11214-004-1435-z.

Stacey, N., and D'Amico, S., "Autonomous swarming for simultaneous navigation and asteroid characterization," *AAS/AIAA Astrodynamics Specialist Conference*, Paper AAS 18-448, 2018.

Streetman, B., Shoer, J., Stoner, R., Peck, M., Manchester, Z., and Weis, L., "Exploration architecture with quantum inertial gravimetry and in-situ ChipSat sensors," *NIAC Phase I final report*, 2015.

Velásquez-Garcia, L. F., Akinwande, A. I., and Martinez-Sanchez, M., "A Planar Array of Micro-Fabricated Electrospray Emitters for Thruster Applications," *Journal of Microelectromechanical Systems*, Vol. 15, No. 5, 2006, doi: 10.1109/JMEMS.2006.879710.

Wang, J., Mohanty, S., Jevremovic, T., Misra, M., Franz, B., Burnham, S., and Kink, T., "CubeSat with Nanostructured Sensing Instrumentation for Planetary Exploration," *NIAC Phase I final report*, 2015.

Werner, S. C., Harris, A. W., Neukum, G., and Ivanov, B. A., "The Near-Earth Asteroid Size–Frequency Distribution: A Snapshot of the Lunar Impactor Size–Frequency Distribution," *Icarus*, Vol. 156, No. 1, 2002, pp. 287–290. doi:10.1006/icar.2001.6789.

Wu, C., "Towards linear-time incremental structure from motion," *2013 International Conference on 3D Vision*, 2013, doi: 10.1109/3DV.2013.25.

Zellner, B., Tholen, D. J., and Tedesco, E. F., "The Eight-Color Asteroid Survey: Results for 589 Minor Planets," *Icarus*, Vol. 61, No. 3, 1985, pp. 355–416, doi:10.1016/0019-1035(85)90133-2.

Zimmerman, M. I., Farrell, W. M., and Poppe, A. R., "Grid-free 2D plasma simulations of the complex interaction between the solar wind and small, near-Earth asteroids," *Icarus*, Vol. 238, 2014, pp. 77–85, doi: 10.1016/j.icarus.2014.02.029.